Grain boundary design based on fractal theory to improve intergranular corrosion resistance of TWIP steels

Hao Fu [a], Wei Wang [a], Xiaojun Chen [b,*], Giorgio Pia [c], Jinxu Li [a,**]

[a] Corrosion and Protection Center, Institute of Advanced Materials and Technology, University of Science and Technology Beijing, Beijing, 100083, China
[b] Key Laboratory of Tectonics and Petroleum Resources, Ministry of Education, China University of Geosciences, Wuhan, 430074, China
[c] Dipartimento di Ingegneria Meccanica, Chimica e Dei Materiali, Università Degli Studi di Cagliari, Via Marengo 2, 09123, Cagliari, Italy

HIGHLIGHTS

- Grains size distribution of TWIP steel satisfies double fractal feature where 36 μm is the diameter threshold of fine grain and coarse grain size.
- RGB, Σ3 GB and GBN of TWIP steel meet multifractal feature.
- Σ3 GB controls the distribution characteristics and complexity of GBN.
- There is a remarkable relationship between thickness loss of corrosion and fractal parameter of Σ3 GB: $h = 0.27t\text{-}37.5\Delta\alpha\text{-}8.88D_{g1}+24.33$.
- GB types and structural parameters with high IGC resistance are predicted based on fractal theory.

GRAPHICAL ABSTRACT
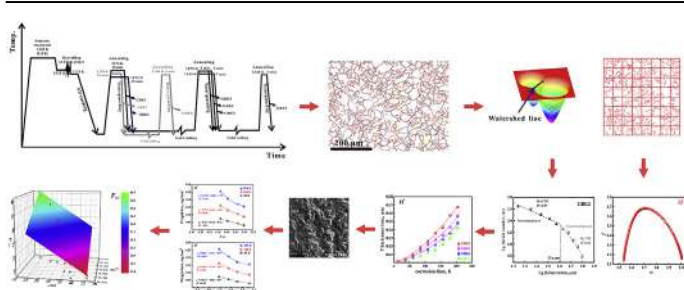
ABSTRACT

The grain size in TWIP steel had a double fractal distribution, with a uniform diameter threshold of approximately 36 μm. Based on this threshold value, the grains were divided into fine and coarse grain sets. A good linear relationship was found between the fractal dimension of the fine grain set (D_{g1}) and the fraction of Σ3 gain boundaries (GBs) ($F_{\Sigma3}$). The distribution characteristics of the three types of GBs satisfy multifractal and generalized fractal characteristics. Importantly, the fractal structural parameters of the Σ3 GBs control the distribution characteristics and complexity of the total grain boundary network (GBN). Combined corrosion test, a quantitative relationship between the corrosion thickness loss and the Σ3 GBs fractal parameter as well as corrosion time was established. In the end, the optimal microstructure characteristics for improving the intergranular corrosion resistance of TWIP steel are discussed from the GB perspective. GB design based on fractal theory provides a promising solution to optimize material corrosion properties through analyzing complex GBN.

© 2019 The Authors. Published by Elsevier Ltd. This is an open access article under the CC BY-NC-ND license (http://creativecommons.org/licenses/by-nc-nd/4.0/).

1. Introduction

The term grain boundary engineering (GBE) could be traced back to the concept of grain boundary (GB) design and control proposed by Watanabe [1] in 1984. Its purpose is to improve the material properties associated with GBs, such as resistance to stress

* Corresponding author.
** Corresponding author.
E-mail addresses: chenxj@cug.edu.cn (X. Chen), jxli65@ustb.edu.cn (J. Li).

corrosion cracking [2–4], creep [5] and hydrogen-induced delayed cracking [6–8], by increasing the fraction of the *special* GBs and controlling the grain boundary characteristic distribution (GBCD) [1] using thermo-mechanical treatment. The so-called special boundary is a GB with a small free volume and a high lattice density in its atomic structure, usually referred to the low-Σ ($1 < \Sigma \leq 29$) coincidence site lattice (CSL) [9], exhibits good performance in effectively suppressing GB segregation and diffusion [10,11]. GBCD refers to the length fraction of low-ΣCSL GBs to total GBs.

It is well known that the GB is directly related to grains distribution, phase structure, etc. And hence to the macroscopic properties of materials [12–16], such as fracture and corrosion [17,18]. Especially for austenitic materials, intergranular corrosion (IGC) is one of the main failure modes [19–21]. Evidence from electrochemistry provides insight into this microscopic mechanism: due to the separation of chemical elements and the disorder of microscopic atoms that are prone to occur at GBs, IGC is commonly caused by differences in chemical composition and electrochemical potential between the GBs and matrix when the surface of the metal contacts the electrolyte solution [22,23]. To suppress this unexpected IGC, GBE is considered to improve IGC resistance. Xia et al. [24] successfully obtained samples with different fractions of low-Σ CSL GBs to study the IGC properties of 690 alloy. Michiuchi et al. [25] characterized the topological characteristics of low-ΣCSL GBs and found that the sensitivity of IGC was significantly reduced when the fraction of low-Σ CSL GBs exceeded 82%. Pradhan et al. [26] found that greater quantities of $\Sigma3^n$ ($n = 1,2,3$) type GBs in 304 L stainless steel can significantly improve their resistance to IGC. Hu et al. [27] found that grain clusters surrounded by random grain boundaries (RGBs) have a beneficial effect on resistance IGC.

From these reviews, the current objective of GBE design for improving IGC resistance is mainly to control the fraction of low-Σ CSL GBs (especially $\Sigma3^n$ type GBs where $\Sigma9$ and $\Sigma27$ are primary and secondary variants of the $\Sigma3$ GB) or RGB, which belongs to the high-ΣCSL GB. Due to the limitations of conventional analytical methods based on experimental data regarding electron backscatter diffraction (EBSD), the GB structure is usually expressed as the fraction of GBs lengths. However, whether low-Σ CSL GBs or RGBs, they all have complex morphologies on a plane or in space. Only a *fraction* of one type of GB is not sufficient to characterize such complex distributions. Thus, it is necessary to quantitatively characterize the complex distribution of GBN to establish some quantitative relationships between their structural parameters and the IGC properties.

The complex grain boundaries network (GBN) is not a regular straight line, but has a very tortuous shape. Classic Euclidean geometry is unable to describe such complex GBN. To quantitatively characterize highly irregular GBs, Non-Euclidean geometry (fractal theory) was introduced in this study. Since the Mandelbrot [28] first applied fractal geometry to the field of materials science in 1984, many studies of fractals have been reported in materials science [29–32]. In our previous work, based on multifractal theory, an important clue to analyze the hydrogen-induced fracture of engineering structural materials was presented [33]. The macroscopic flow and heat transfer properties of porous materials were also quantitatively modeled [34–39]. Recently, Kobayashi et al. [10,40] analyzed the characteristics of RGBs based on fractal geometry and found that the fractal dimension of RGBs increases with increasing RGB fraction. Pradha et al. [26,41] found that high fractal dimensions correspond to large RGBs with high connectivity, which is detrimental to IGC. However, few studies have reported on the IGC resistance of $\Sigma3^n$ (especially $\Sigma3$) GBs occupying the largest fraction in the low-Σ CSL GBs. Additionally, the grain size distribution affects the GBCD. Generally, the grain size is characterized by the average and bimodal average grain size [42]. However, the average grain diameter does not describe the total grain size

distribution, and a more accurate parameter is needed to characterize grain size distribution. Thus, detailed quantitative analyses $\Sigma3$ GBs and grain size distribution based on fractal theory are very desirable.

In recent years, TWIP steels have become a candidate material in many fields, such as the automotive industry, liquefied natural gas shipbuilding, and petroleum and natural gas exploration [43], due to their good comprehensive mechanical properties [44–46]. However, TWIP steels used in industrial, marine and H_2S environments will suffer severe corrosion and the method for improving its corrosion resistance is limited to anti-corrosion coatings and addition of alloying elements [47–51]. Therefore, controlling IGC based GB design is an alternative route. In this study, TWIP steel samples with different GB types are first obtained by thermo-mechanical treatment. Then, the fractal characteristics of grain size and GB distribution are explored based on the fractal theory. More importantly, the relationship between the structure parameters of GB and the corrosion performance was established combined with the IGC test. This study could provide guidance for optimizing the GB design, improve corrosion resistance and extend the service life of TWIP steels as well as provide useful information and value for automotive steel and other related research.

2. Experiments and methods

2.1. Thermo-mechanical treatment process

The chemical composition of the TWIP steels used for testing was Fe-18Mn-0.6C (Table 1). This test steel was melted under an argon atmosphere in a vacuum induction furnace and was then cast into a 21 kg ingot after melting. The ingot was forged at $0.855\Theta H$ (1423 K) for 1.5 h and then was forged into a $900 \times 100 \times 40\ mm^3$ bulk. The starting temperature for ingot forging is $0.855\Theta H$ (1423 K) and the termination temperature is $0.766\Theta H$ (1275 K). The chosen temperatures were expressed by homologous temperatures $\Theta H = T/T_m$, where the T_m (K) is the melting point (1664 K), and T (K) is the experimental temperature. The ingot was initially cylindrical and has a diameter of 150 mm and a height of 300 mm. To prevent oxidative decarburization on the surface of the ingot during forging, a kind of commercial anti-oxidant coating, Type Century-1, was brushed to the ingot surface with a layer thickness of ~0.2 mm. The steel bulk painted with the anti-oxidation coating was hot rolled (starting temperature was $0.80\Theta H$ (1323 K), final rolling temperature was greater than $0.70\Theta H$ (1173 K)) to 3.6 mm, followed by air-cooling to room temperature, and then the surface iron oxide scale was removed by grinding method. To obtain different GB types samples, GBE design was completed by changing the processing parameters (e.g., temperature and time). First, the hot-rolled samples were subjected to solution treatment at different temperatures. The solution temperatures for the three samples were 1273 K ($0.765\Theta H$), $0.75\Theta H$ (1248 K) and $0.735\Theta H$ (1223 K). The samples were kept at $0.765\Theta H$ (1273 K) and at $0.75\Theta H$ (1248 K) for 10 min and at $0.735\Theta H$ (1223 K) for 15 min, respectively. Afterwards, the samples were all water quenched to room temperature. The three samples were named as follows: GBE1 ($0.765\Theta H$ (1273 K), 10 min), GBE2 ($0.75\Theta H$ (1248 K), 10 min) and GBE3 ($0.735\Theta H$ (1223 K), 15 min), respectively. Second, many GBE1 samples were subjected to cold rolling with a reduction of 5% of thickness from the initial thickness of 1.80 mm to the final

Table 1
Chemical composition analysis of the steel investigated in the present study (wt. %).

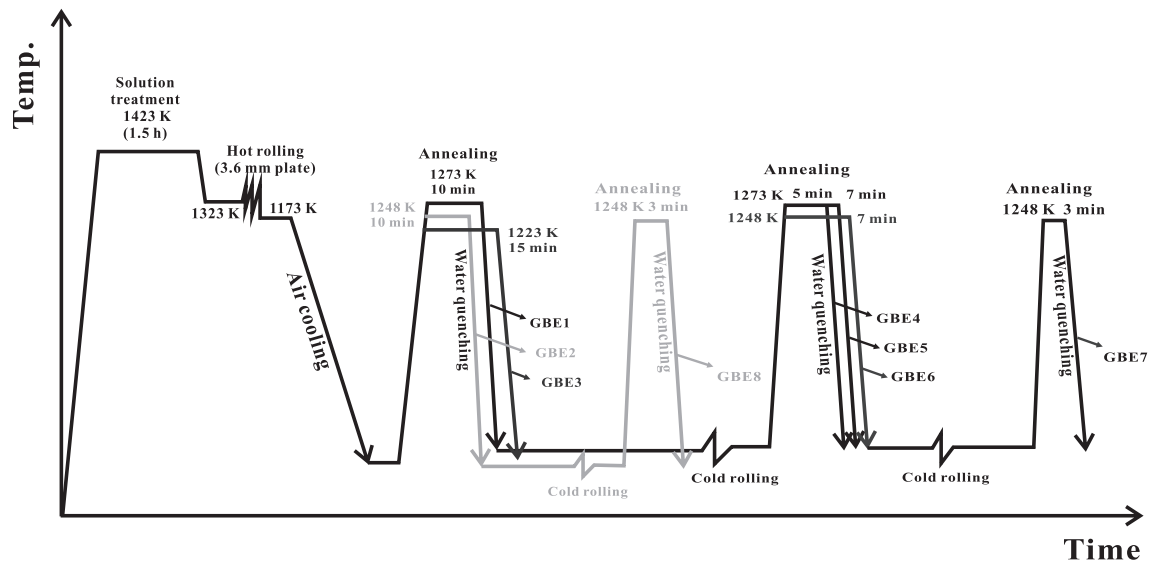| Mn	C	S	P	Fe
18.2	0.56	0.006	0.008	Balance.

Fig. 1. Schematic showing rolling and heat treatment processes.

thickness of 1.71 mm. Some of cold-rolled GBE1 samples were then annealed at 0.765ΘH (1273 K) for 5 min or 7 min, respectively, for GBE4 and GBE5, followed immediately by water quenching to room temperature. The other cold-rolled GBE1 samples were annealed at 0.75ΘH (1248 K) for 7 min, followed by water quenching to room temperature, called as GBE6. Next, some GBE6 samples were again subjected to 5% reduction by cold rolling and annealed at 0.75ΘH (1248 K) for 3 min followed by water quenching to room temperature, called as GBE7. Finally, some GBE2 samples were subjected to 5% reduction of thickness by cold rolling from the initial thickness of 1.80 mm to the final thickness is 1.71 mm and then annealed at 0.75ΘH (1248 K) for 3 min, followed by water quenching to room temperature, called as GBE8. The detailed thermo-mechanical process is shown in Fig. 1. Table 2 summarizes all the processing steps performed for all GBE samples. The entire heat treatment process is completed in an argon atmosphere.

2.2. GB characterization

To observe the GB microstructure of the TWIP steels, the GBE (1−8) series of samples were first polished with 300−5000# metallographic sandpaper and followed by polishing with 1.5 μm diamond polishing pastes. After mechanical polishing, electro-polishing was performed with 10% perchloric acid +90% acetic acid. The temperature is 298 K. The voltage is 22 V. The sample size is $10 \times 8 \times 1.5$ mm^3. The sample is sandwiched by the tweezers for 20 s. The cathode material is 304 stainless steel. The distance between the electrodes is 3 mm. All samples were characterized by a focused ion beam field emission electron microscope (FE-SEM

ZEISS DSM) with an electron backscatter diffraction (EBSD) detector after electropolishing. The operating voltage was 20 kV, and the working distance was 17.0 mm. The EBSD scan step size is 1.0 μm. The EBSD data were processed by Channel 5 software. In this work, according to Brandon's standard [52], $\Delta\theta_{max} = 15°\Sigma^{-5/6}$, the GB of $1 < \Sigma \leq 29$ is defined as the CSL GB.

2.3. Corrosion tests

Four types of samples were selected from the GBE (1−8) series of TWIP steels (the selection principle will be described in detail in Section 3.3). Four selected samples with a size of 18 mm × 16 mm × 1.5 mm were wire-cut to prepare for corrosion testing. In the corrosion test, nine samples were prepared for each type of GBE sample in the corrosion test. There are four types of GBE2, GBE5, GBE6 and GBE8, hence, a total of 36 test samples in each corrosion environment. Then, all samples were mechanically polished to obtain a clean surface. The surface area for each sample was measured by vernier caliper and the weight of each sample was also measured by analytical balance (where the weight accuracy reaches 0.1 mg). The average value and the standard deviation were calculated. The solutions used in the corrosion test were 0.05‰ sulfuric acid +0.1 g/L iron sulfate solution (pH = 4.5) and 3.5% sodium chloride solution (pH = 7), the pH measurement error is ±0.001 and the purity of the reagents in both solutions is analytically pure (Analytical Reagent). The closed polypropylene plastic box was selected as the corrosion test container. Each sample is suspended in a container. The temperature during the corrosion soaking process was 298 K, and the test environment was a

Table 2
Summarizes all the processing steps performed for all GBE samples.

| Sample Name	Step1	Step2	Step3	Step4	Step5	Step6	Step7
GBE1	Solution treatment 1423 K in 1.5 h	Hot rolling	Annealing 1273 K in 10 min	−	−	−	−
GBE2	Solution treatment 1423 K in 1.5 h	Hot rolling	Annealing 1248 K in 10 min	−	−	−	−
GBE3	Solution treatment 1423 K in 1.5 h	Hot rolling	Annealing 1223 K in 15 min	−	−	−	−
GBE4	Solution treatment 1423 K in 1.5 h	Hot rolling	Annealing 1273 K in 10 min	Cold rolling	Annealing 1273 K in 5 min	−	−
GBE5	Solution treatment 1423 K in 1.5 h	Hot rolling	Annealing 1273 K in 10 min	Cold rolling	Annealing 1273 K in 7 min	−	−
GBE6	Solution treatment 1423 K in 1.5 h	Hot rolling	Annealing 1273 K in 10 min	Cold rolling	Annealing 1248 K in 7 min	−	−
GBE7	Solution treatment 1423 K in 1.5 h	Hot rolling	Annealing 1273 K in 10 min	Cold rolling	Annealing 1248 K in 7 min	Cold rolling	Annealing 1248 K in 3min
GBE8	Solution treatment 1423 K in 1.5 h	Hot rolling	Annealing 1248 K in 10 min	Cold rolling	Annealing 1248 K in 3min	−	−
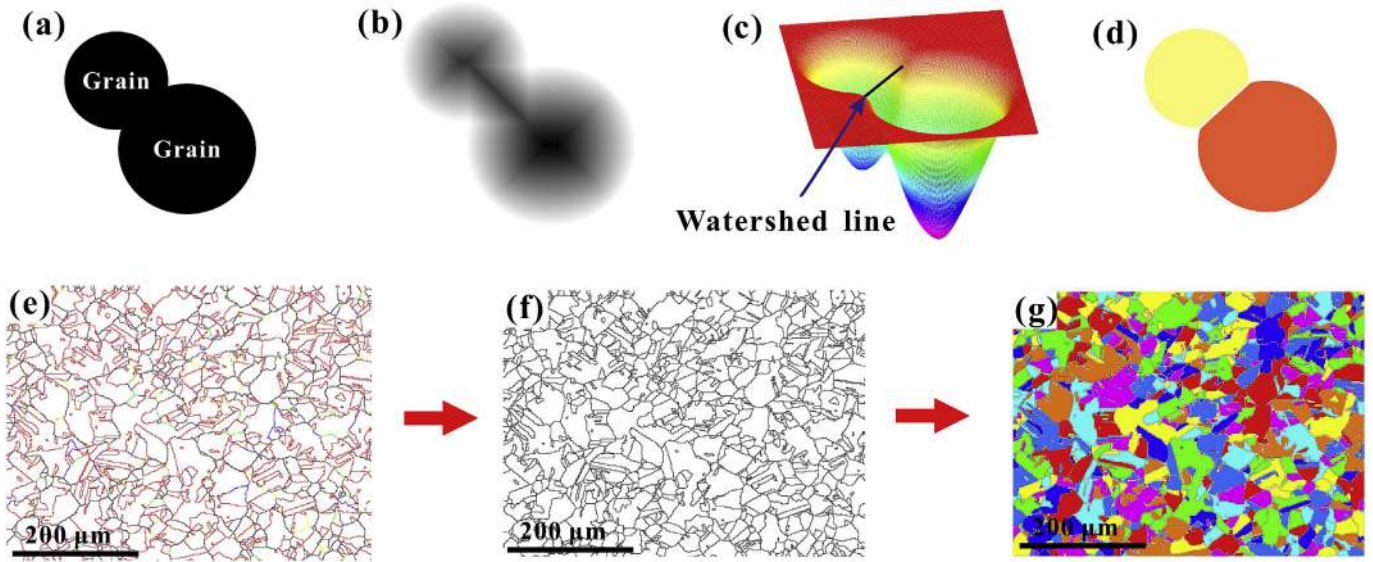
Fig. 2. Schematic for watershed segmentation algorithms: (a) two connected circular grains; (b) distance map after *City-block* transformation; (c) color depth map from (b); (d) grains segmented by a watershed line in (c); (e) global GB network of GBE2; (f) Binary global GB network; and (g) segmented result from (f).

laboratory environment. A 20 mL solution was used per square centimeter of sample. The samples were taken out every 24 h, washed 3 times in water and then washed twice in alcohol. The samples were dried with a hair dryer after each wash. Each sample was then weighed again to obtain corrosion mass loss. The corrosion test in this work was performed for a total of 204 h to obtain a corrosion weight loss curve. The surface morphology of each sample after corrosion was observed by SEM with an accelerating voltage of 20 kV.

2.4. Grain size fractal dimensions

From the complex GBN, the grain size is not constant but has a specific distribution. As we know, the grains are separated by GBs. Additionally, the shape of the grain is very irregular. To calculate the number and size distribution of grains in the EBSD image of each sample, a watershed segmentation algorithm was used to extract individual grains. Rash et al. [53] discussed in detail the effects of distance types (Euclidean, City-block, Chessboard, Quasi-Euclidean) on sandstone particle segmentation in thin sections. City-block distance was considered to be optimal and was thus chosen for this analysis. The results of the segmentation are shown in Fig. 2 for the GBE samples, where different grains are marked with different colors (Fig. 2(g) is different from the inverse pole figure (IPF) of the EBSD). Afterwards, the pixel area of each grain was counted. Finally, according to the principle of area equivalent, the diameter of the circle with the same pixel area was calculated as the diameter of the corresponding grain. Similar to a single fractal dimension, here D_g was defined the fractal dimension of grain size distribution, which is expressed as [39]:

$$N_t(\geq d) = d^{-D_g} \tag{1}$$

where d is the grain diameter, and N is the cumulative number of grains with a diameter larger than d. Detailed analysis of the eight samples will be discussed in section 3.2.

2.5. GB extraction and fractal dimension

Our previous work concluded that a single fractal dimension does not adequately characterize the roughness of fracture surfaces.

However, multifractal and generalized fractal approaches can complement this deficiency.

To calculate in detail the proportion p_i of GB pixels in each box, the generalized entropy function $H_q(\delta)$ is defined as:

$$H_q(\delta) = \frac{\ln \sum\limits_{i=1}^{N} p_i^q}{1 - q} \tag{2}$$

where δ is the box size; p_i is the ratio of GB pixels in the i-th box; p_t denotes the total number of pixels in the box; p_i represents the total number of GB pixels; and N denotes the total number of boxes. The constant q usually varies between −10 and 10 in increments of 1. Based on $H_q(\delta)$, the generalized dimension D_q (also known as the Renyi dimension) is defined as [54]:

$$D_q = -\lim_{\delta \to 0} \frac{H_q(\delta)}{\ln \delta} = \frac{\tau(q)}{q-1}; \left(q = 1, D_1 = \frac{\sum p_i \ln p_i}{\ln \delta} \right) \tag{3}$$

The curve shape of $\tau(q)$-q determines whether the calculated structure meets the multifractal law. For a mathematically strict self-similar fractal pattern, the D_q value does not change with q and is always equal to D_0 (Eq. (3)). However, objects in nature are not perfectly self-similar, such as GBN, which causes the D_q to change with q. Commonly, D_q reaches its minimum value ($D_{\min}$) with $q = -10$. Similarly, D_q reaches its maximum value ($D_{\max}$) with $q = 10$.

In multifractal theory, p_i is also considered. The multifractal spectrum is defined as follows [55]:

$$f(\alpha) = -\lim_{\delta \to 0} \frac{\ln(N_p)}{\ln(\delta)}$$

$$\alpha(q) = \lim_{\delta \to 0} \frac{\ln(p_i)}{\ln(\delta)} \tag{4}$$

where $\alpha(q)$ is the singularity index; $f(\alpha)$ represents the multifractal spectrum as a fractal dimension of a subset with the same α; and N_p denotes the number of subsets with the same probability p_i. Through the Legendre transformation, $f(\alpha)$ and $\alpha(q)$ can be rewritten as:

$$\alpha(q) = \frac{\partial \tau(q)}{\partial q} \tag{5}$$

$$f(q) = \alpha(q)q - \tau(q)$$

As mentioned above, $\tau(q)$ represents the indicator of a multifractal feature. Combined with the definition of $\tau(q)$, Eq. (5) can be rearranged as:

$$\alpha(q) = \lim_{\delta \to 0} \frac{1}{\ln \delta} \sum_i \mu_i \ln(p_i)$$

$$f(q) = \lim_{\delta \to 0} \frac{1}{\ln \delta} \sum_i \mu \ln(\mu_i) \tag{6}$$

where the $\mu_i = p_i^q / \sum p_i^q$ [55]. The plot of $f(\alpha)$ against α is the known multifractal spectrum curve [56]. Thus, based on the box counting algorithm, to calculate the multifractal and generalized fractal dimensions of a certain type of GB, that type must be extracted from the total GBN. Typically, the total GBN contains five colors and hence is a typical two-dimensional color image. Thus, based on the color extraction algorithm, RGBs and $\Sigma 3$ GBs were extracted separately from the total GBN (Fig. 3(a)). To continuously subdivide the SEM image, the image size of the image used to calculate the fractal dimension must be 2^N pixel. A maximum subarea of 512×512 pixels was extracted from the original image containing different GB types (Fig. 3(b$_{1-3}$ and c$_{1-3}$)). Finally, multifractal and generalized fractal parameters of all images were calculated (Fig. 3(d$_{1-3}$ and e$_{1-3}$)).

2.6. Average corrosion thickness

For the IGC test, the average corrosion thickness can be used to estimate the number of grain layers that are corroded. If the average corrosion thickness is less than the average grain diameter, the first layer of grains on the sample surface is not completely corroded. The average corrosion thickness was also indirectly estimated as shown in Fig. 4(a and b).

Here, since the sample is completely immersed in the solution, the corrosion rates of the six outer surfaces of the sample are approximately equal. After the sample has been corroded for time t, the mass loss Δm can be expressed as:

$$\Delta m = \Delta v \cdot \rho = (\overline{A} \cdot \overline{B} \cdot \overline{H} - (\overline{A} - h)(\overline{B} - h)(\overline{H} - h)) \cdot \rho \tag{7}$$

where h is the average corrosion thickness, and $\overline{A}$, $\overline{B}$, and $\overline{H}$ denote the initial average side lengths (length, width and height), respectively. The initial mass of sample is M_o, and thus the density ρ of sample can be expressed as:

$$\rho = \frac{M_o}{\overline{A} \cdot \overline{B} \cdot \overline{H}} \tag{8}$$

Combining Eq. (7) with Eq. (8), based on the original physical lengths and weight loss data of the tested sample, the average corrosion thickness can be solved analytically. It can be seen from Fig. 4(c and d) that the theoretical estimated data from Eqs. (7) and (8) are almost equal to the experimentally measured data from SEM images.

3. Results and discussion

3.1. Evolution of GB microstructure

The microstructure of TWIP steel will evolve as it undergoes recrystallization during the thermo-mechanical treatment. Fig. 5 shows the EBSD images of the GBE series samples. The GB distribution images of each sample are presented in Fig. 5(a$_1$-h$_1$) and indicate that the GBN in each sample exhibits diverse combinations of different types of GBs. Specifically, abundant $\Sigma 3$ (red), $\Sigma 9$ (blue) and $\Sigma 27$ (green) GBs are agglomerated together. Furthermore, $\Sigma 3^n$ (n = 1, 2, and 3) GBs are connected to each other to form many nodes of three GBs, such as $\Sigma 3$-$\Sigma 3$-$\Sigma 9$ and $\Sigma 3$-$\Sigma 9$-$\Sigma 27$. Most of these nodes are in areas surrounded by RGBs (black), which is most
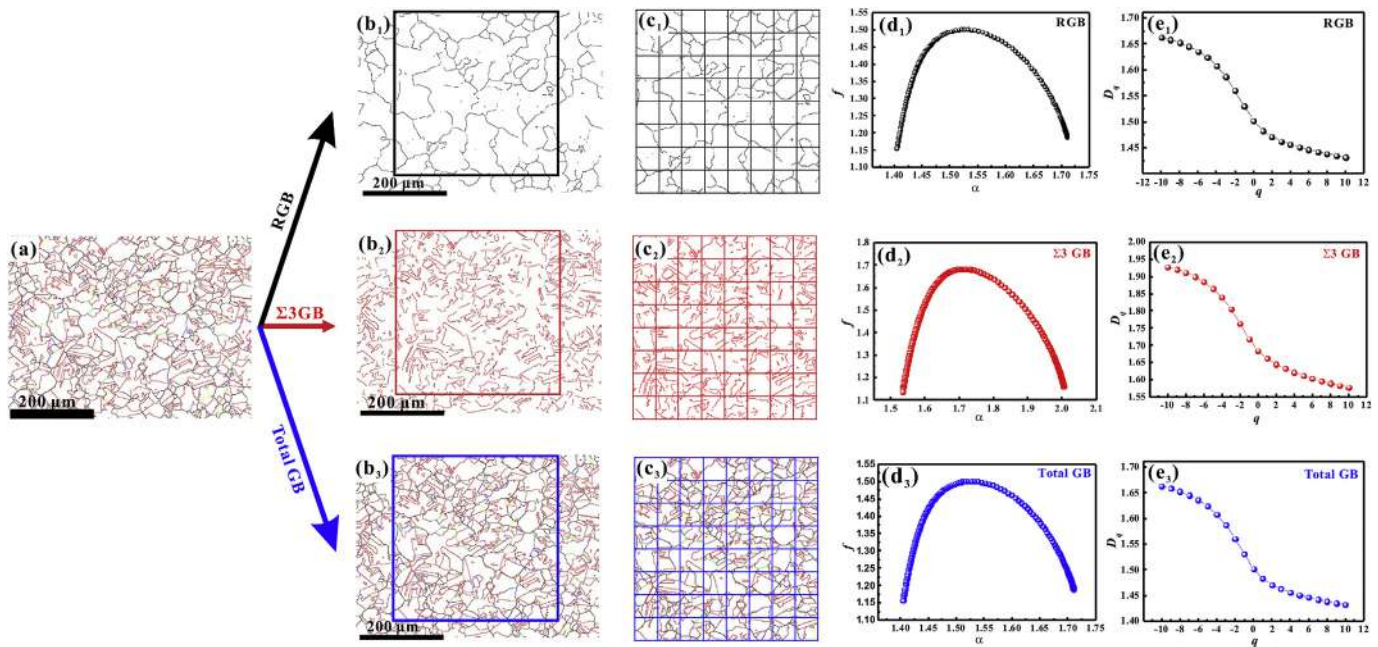

Fig. 3. Process of obtaining generalized fractal and multifractal parameters from the original GB map from EBSD image: (a) original GB image of GBE2; (b) extraction of three main GBs (b$_1$-RGB, b$_2$-$\Sigma 3$, b$_3$-total GBN); (c) selection of the largest computed subarea from (b), with a size of 512×512 pixels, and the covered 8×8 grid for the BC algorithm; (d) calculation of the multifractal spectrum from the binary (c) for the three main GB types; and (e) calculated the generalized fractal spectrum from the binary (c) for the three main GB types.
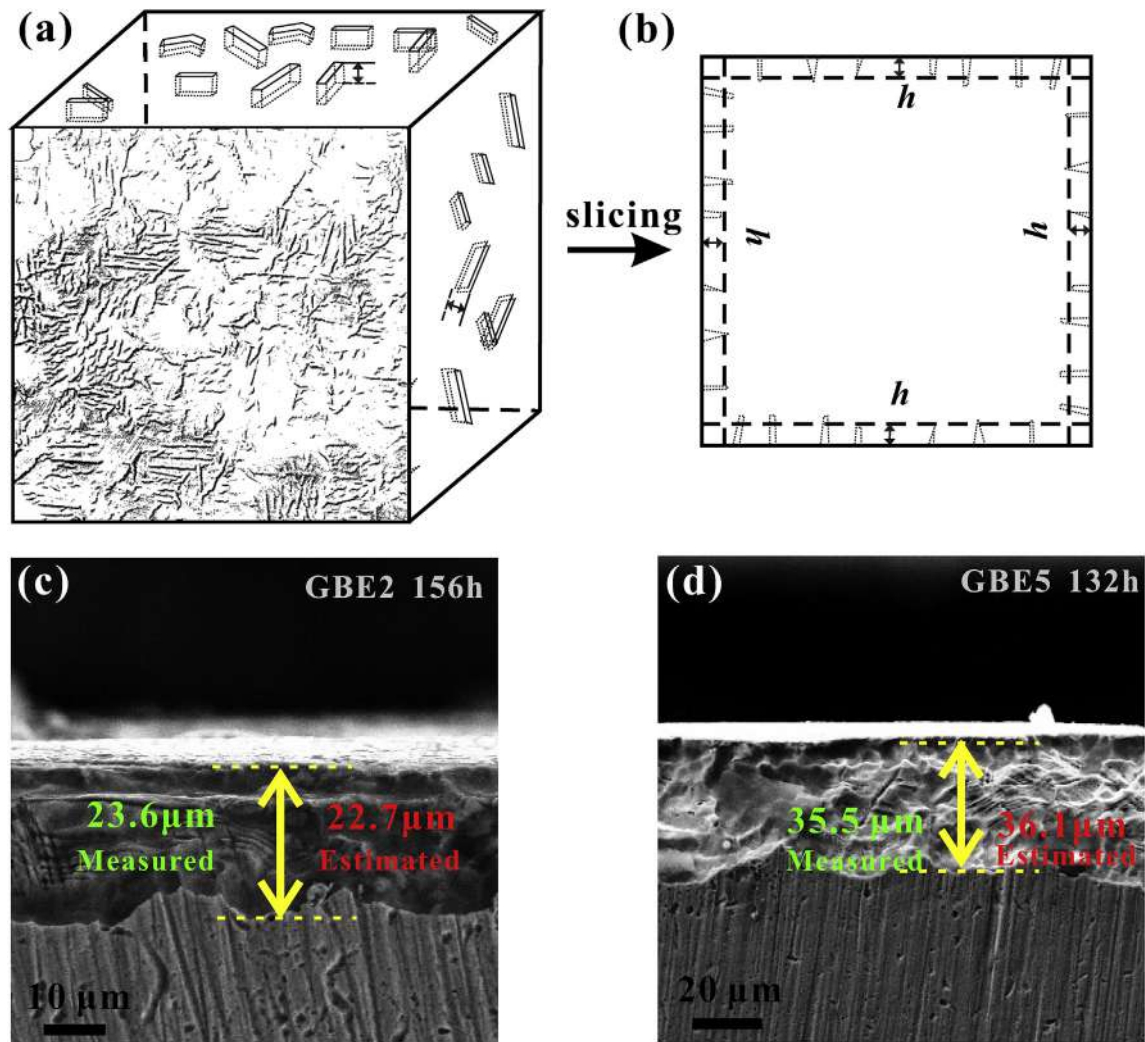
Fig. 4. Schematic for calculating the average corrosion thickness h: (a) the rough surface of the cubic sample after IGC test, where the matrix is more severely corrosion; (b) one slice comes from (a) with the average corrosion thickness loss of h; (c) the SEM images of the GBE2 sample at 156 h; (d) the SEM images of GBE5 sample at 132 h (The green numbers are the measured data, and the red numbers are theoretically estimated data).

evident in GBE2 (Fig. 5b$_1$). As mentioned in the introduction, The GBE is designed to increase the fraction of low-ΣCSL GBs and minimize the fraction of RGBs (F_R). For low-ΣCSL GBs, the $\Sigma 3^n$ type GB occupies a dominant position, and the $\Sigma 9$ and $\Sigma 27$ GBs are the second and third variants of the $\Sigma 3$ GB within the $\Sigma 3^n$ type GB. Thus, the fractions of the $\Sigma 9$ and $\Sigma 27$ GBs are very small, which indicates that the fraction of $\Sigma 3$ GBs ($F_{\Sigma 3}$) in the $\Sigma 3^n$ type GB is considerable. In this way, for the total GBN, the main GB types are $\Sigma 3$ and RGB. Thus, the configuration changes of the $\Sigma 3$ GBs and the RGBs are analyzed in this work. The IPF images of each pattern is in the lower left corner of Fig. 5(a$_1$-h$_1$). According to the IPF images, the grain orientation of each sample tends to be randomly distributed, which indicates that the TWIP steel has no obvious microtexture. Thus, the influence of the microtexture of the GB microstructure on corrosion properties can be further excluded.

Table 3 shows the length fraction of different types GBs and average grain sizes (diameter) in the GBE series samples. The fractions of $\Sigma 3^n$ type GB in the all GBE samples vary between 10% and 50%, with GBE2 having the highest (reaches ~47.29%) and GBE5 having the lowest (~15.17% only). Similarly, for the $\Sigma 3$ GB, the $F_{\Sigma 3}$ is also the highest (up to 40.69%) in the same sample (GBE2), and GBE5 also has the lowest (~13.40% only). For RGBs, the F_R of GBE2 was the lowest (51.99%), and that of GBE5 was the highest (83.11%).

The samples with different fractions of GBs ($\Sigma 3^n$ and RGB) were obtained by thermo-mechanical treatment of TWIP steel. The average grain diameter did not change significantly (maximum in GBE1: 29.7 μm, and minimum in GBE2: 24.6 μm). Pradhan et al. [26] reported that the average grain size and the residual stress on the surface also affect the corrosion properties of structural materials in addition to the GB type. Thus, the influence of average grain size on the corrosion performance of the sample can be excluded. Additionally, the kernel average misorientation (KAM) values of all the GBE samples were small from the KAM diagram, as shown in Fig. 5(a$_2$-h$_2$), indicating that the residual stress on the surface of all the GBE samples was equivalent, and the influence of the residual stress on the corrosion property can be further ignored.

3.2. Fractal analysis of grain size distribution and GBN

Polycrystals are formed by spatially arranging individual grains. The size and shape of each crystal grain are not exactly the same. Statistically, any part is similar to the total. Therefore, whether the crystal grains satisfy the self-similar characteristics can be visually judged. In this section, the grain size distribution and GBN characteristics of TWIP steels will be analyzed in detail based on fractal theories.
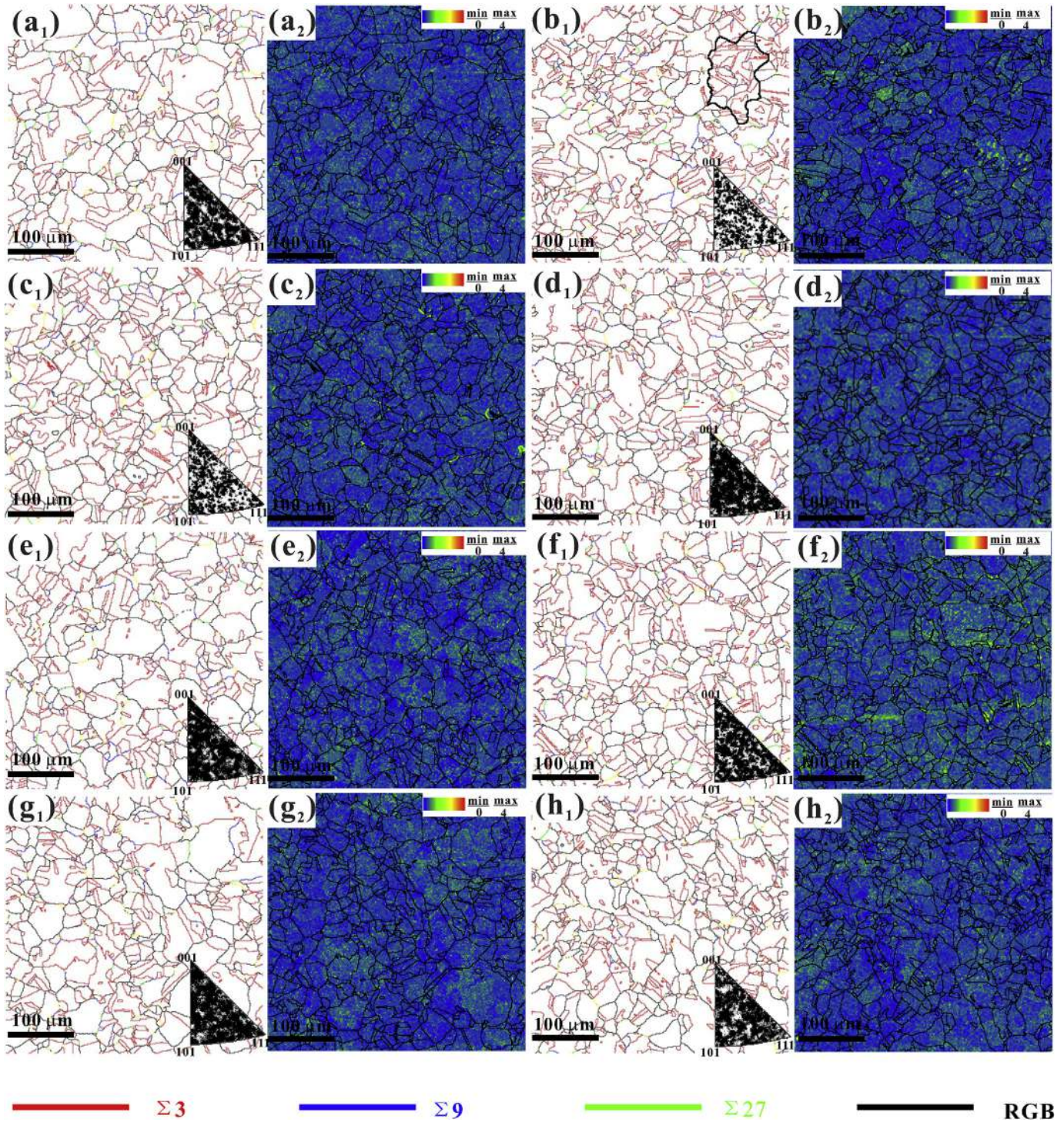
Fig. 5. Microstructure distribution characteristics of GBE (1−8) series samples: (a₁-h₁) is the distribution images of the GB network (the IPF diagram of each pattern is in the lower left corner of the GB map); (a₂-h₂) is the kernel average misorientation (KAM) map; and ((a−h) corresponds to the GBE (1−8) samples in turn).

3.2.1. Fractal characteristics of grain size distribution

The grain size distribution of all EBSD images were found using a watershed transformation algorithm with city-block distance (see Section 2.4 for details), and the grain size distribution of all samples were calculated. Fig. 6 shows a double logarithmic plot of the cumulative number of grains versus grain diameter in each GBE sample. According to Section 2.4, the grain fractal dimension D_g can be obtained by fitting data points in Fig. 6. The high fitting coefficient ($R^2 > 0.99$) indicates that the grain size distribution satisfies the double fractal (also known as bifractal) feature, which further indicates that the total grain set can be divided into two subsets, fine and coarse grain sets, in each sample, each exhibiting different size distribution characteristics, as shown in Fig. 6. Namely, two fractal dimensions, D_{g1} and D_{g2}, describe the full grain size distribution within one sample. Interestingly, the critical grain diameter (d_c) at the boundary between the fine grain set and the coarse grain set is approximately 36 μm, i.e., the mean value of all the GBE (1−8) samples. The detailed D_{g1}, D_{g2} and d_c values of all GBE sample are

Table 3
Fraction of different types of GBs $\Sigma 3^n$ (n = 1, 2, and 3) and RGBs) and average grain diameter (d_{mean}) for all GBE samples.

Sample No.	$F_{\Sigma 3}$ (%)	$F_{\Sigma 9}$ (%)	F_{27} (%)	F_R (%)	d_{mean} (μm)
GBE1	24.08	3.04	1.25	70.21	29.7
GBE2	40.69	4.47	2.13	51.99	24.6
GBE3	36.16	2.77	1.18	59.12	25.1
GBE4	28.01	2.42	0.69	67.26	26.2
GBE5	13.40	1.43	0.34	83.11	26.8
GBE6	30.42	3.39	1.16	65.27	24.8
GBE7	17.29	1.51	0.44	79.04	26.0
GBE8	21.53	1.41	0.38	74.96	25.8

summarized in Table 4.

As the d_c increases, the number of grains in the fine grain set decreases at a slower rate than that of the coarse grain set (that is, $D_{g1}<D_{g2}$), as shown in Fig. 6. Commonly, abundant twins in samples were formed in the thermo-mechanical treatment, and these twins generally extended toward the inside of the austenite grains. When the grains shown in the EBSD images were segmented, the twins are recognized as one grain in calculating D_{g1} and D_{g2}. This indicates that twins contribute a considerable fraction of the total number of grains in the fine grain set. It is well accepted that the twin boundary is a typical $\Sigma 3$ GB, so it can be concluded that the grain fractal dimension of the fine grain set D_{g1} is directly related to the $\Sigma 3$ GB distribution. Fig. 7 shows the relationship between the fractal dimension of grains (D_{g1} and D_{g2}) and $F_{\Sigma 3}$. From Fig. 7(a), D_{g1} and $F_{\Sigma 3}$ satisfy an excellent linear relationship, that is, the higher the value of $F_{\Sigma 3}$, the larger the fractal dimension of the fine grains. However, no correlation is observed between D_{g2} and $F_{\Sigma 3}$, as shown in Fig. 7(b). This further shows that the grain size of TWIP steel is controlled within 36 μm, and more $\Sigma 3$ GBs can be obtained.

3.2.2. Fractal analysis of GBs

Fig. 8 shows that the curves of $\tau(q)$ and q have a nonlinear relationship with an upwardly convex shape, indicating that RGBs, $\Sigma 3$ GBs and total GBN all meet multifractal characteristics.

Generally, the multifractal features of complex objects are characterized by a multifractal spectrum and a generalized fractal spectrum. Fig. 9 shows the multifractal spectrum $f(\alpha)$ (Fig. 9(a, c, e)) and the generalized fractal spectra $D(q)$ (Fig. 9(b, d, f)) of RGB, $\Sigma 3$ GBs and total GBN for the GBE (1−8) series samples. Multifractal spectra of all samples for RGB, $\Sigma 3$ GBs and total GBN are similarly hook-shaped, and the generalized fractal spectra show a "z" shape. In the multifractal spectra, the width of the GBs multifractal spectra ($\Delta \alpha = \alpha_{max} - \alpha_{min}$) is very different; the $\Delta \alpha$ value varies with a fraction of one type of GB. In the generalized fractal spectrum, the corresponding $D(q)$ values when $q = 10$, 0, 1, 2, and −10 are the maximum generalized dimensional value D_{max}, the capacity dimension D_0, the information dimension D_1, and the correlation dimension D_2, respectively. In Fig. 9(b, d, f), the variations of the minimum generalized dimensional D_{min} values of the RGBs, $\Sigma 3$ GB and total GBN are very significant, which indicates that in the GBE series samples, the D_{min} value varies with the fraction of one type of GB. Table 5 summarizes the calculated multifractal and generalized fractal parameters for different GB types in all samples.

To explore the correlation between the complexity of GBs and the fraction of GBs, the relationships between the $\Delta \alpha$ and D_{min} of the RGBs, $\Sigma 3$ GBs and total GBN and their fractions in the GBE series samples are established, as shown in Fig. 10. Although the $\Delta \alpha$ and D_{min} of the RGBs are different from each other in all samples, according to Fig. 10 (a, b), no significant correlation exists between $\Delta \alpha$ or D_{min} and F_R. That is, although the RGBs in each sample satisfy the multifractal characteristics, F_R is not the main factor affecting the complex configuration of GBN. As shown in Fig. 10(c and d), the $\Delta \alpha$

and D_{min} of the $\Sigma 3$ GBs in each GBE sample continuously increased with increasing values of $F_{\Sigma 3}$, with a good linear positive correlation. For $\Delta \alpha$, when the $F_{\Sigma 3}$ is 13.4%, $\Delta \alpha$ equals 0.36, and when the $F_{\Sigma 3}$ increases to 40.69%, $\Delta \alpha$ increases to 0.48. Thus, as the $F_{\Sigma 3}$ increases, the $\Sigma 3$ GBs distributions in the two-dimensional plane and the three-dimensional space become more complicated. Multifractal analysis considers the probability of the $\Sigma 3$ GBs in each box in the box-counting algorithm. When the $\Sigma 3$ GBs becomes more complicated (exhibiting more GBs pixels, more tortuous GBs, and more irregular GB shapes), the probabilities of the $\Sigma 3$ GBs in the boxes become more differentiated. Some boxes are almost filled with pixels of $\Sigma 3$ GBs, and some of the boxes still do not cover the pixels of a $\Sigma 3$ GB. Thus, $\Delta \alpha$ characterizes the total probability distribution of the $\Sigma 3$ GBs in all boxes. When the box size $\varepsilon \leq 1$, the smaller the α_{min} value, the greater the distribution of the large probability subset (the box with a large proportion of $\Sigma 3$ GBs). The larger the α_{max} value, the smaller the distribution of the small probability subset (the box with a small $F_{\Sigma 3}$). The value of α_{max} represents the probability of a small $\Sigma 3$ GB proportional distribution, and α_{min} represents the probability of a large $\Sigma 3$ GBs proportional distribution. Thus, $\Delta \alpha$ can be used to describe the complexity of the $\Sigma 3$ GBs. The larger the value of $\Delta \alpha$, the wider the range of the probability distribution of the $\Sigma 3$ GBs for all boxes, and the greater the difference between the most uniform and the most uneven $\Sigma 3$ GBs probabilities. In contrast, the smaller the value of $\Delta \alpha$, the narrower the proportional distribution of the $\Sigma 3$ GBs in the box, and the smaller the difference between the most uniform and the most uneven $\Sigma 3$ GBs probabilities. Thus, $\Sigma 3$ GBs with large $\Delta \alpha$ values are more abundant and complex, constitute a larger fraction of the total, and have a more irregular corresponding GBs shape.

As mentioned above, when the sample is subjected to thermo-mechanical treatment and a many $\Sigma 3$ GBs are contained (such as GBE2), grain clusters surrounded by RGBs are formed, and GBs inside the cluster are formed. The GBs inside the cluster have $\Sigma 3^n$ relations with each other and exhibit a complex distribution state [13], as shown in Fig. 5(b_1). In this way, the larger the $\Delta \alpha$ value of the $\Sigma 3$ GBs, the more complex the distribution of the $\Sigma 3$ GBs in a certain region (mainly grain cluster). If the $\Delta \alpha$ value of the $\Sigma 3$ GBs is smaller, it indicates that the $\Sigma 3$ GBs have a small degree of complexity in a certain region, as shown in Fig. 5(e_1). Similarly, for D_{min}, when $F_{\Sigma 3}$ is 13.4%, the D_{min} value is 1.80, and when $F_{\Sigma 3}$ reaches 40.69%, D_{min} increases to 1.93. A good positive correlation between D_{min} and $F_{\Sigma 3}$ was found. Since a $\Sigma 3$ GB shows a "linear" object on a two-dimensional plane, its pixels do not fill the entire box in the generalized fractal analysis. Thus, the probability of a $\Sigma 3$ GBs in each box approaches a small probability subset. When $q < 0$, the small probability subset will play a leading role while calculating D_{min}. Thus, D_{min} can be combined with $\Delta \alpha$ to characterize the complexity of the $\Sigma 3$ GBs.

The relationship between the complexity of RGBs and $\Sigma 3$ GBs and their fraction ($F_{\Sigma 3}$, F_R) has been discussed above. Now, we will discuss the influence of RGBs and $\Sigma 3$ GBs on the distribution characteristics of the total GBN to determine which type of GB mainly affects the complexity of the total GBN. Fig. 11 shows the relationships between $\Delta \alpha$ and D_{min} of the total GBN in the GBE series sample and $\Delta \alpha$ and D_{min} of RGBs and $\Sigma 3$ GBs. Fig. 11(a and b) shows no correlations between $\Delta \alpha$ and D_{min} of total GBN and $\Delta \alpha$ and D_{min} of RGBs; that is, the complexity of the total GBN is not related to that of the RGBs. However, Fig. 11(c and d) presents that $\Delta \alpha$ and D_{min} of the total GBN show a good positive correlation with $\Delta \alpha$ and D_{min} of $\Sigma 3$ GBs; the complexity of the total GBN is related to that of the $\Sigma 3$ GBs. In other words, the complexity of the $\Sigma 3$ GBs controls the complexity of the total GBN. To explore the relationship between the structural characteristics of the $\Sigma 3$ GBs and the IGC properties, intergranular corrosion tests were performed.
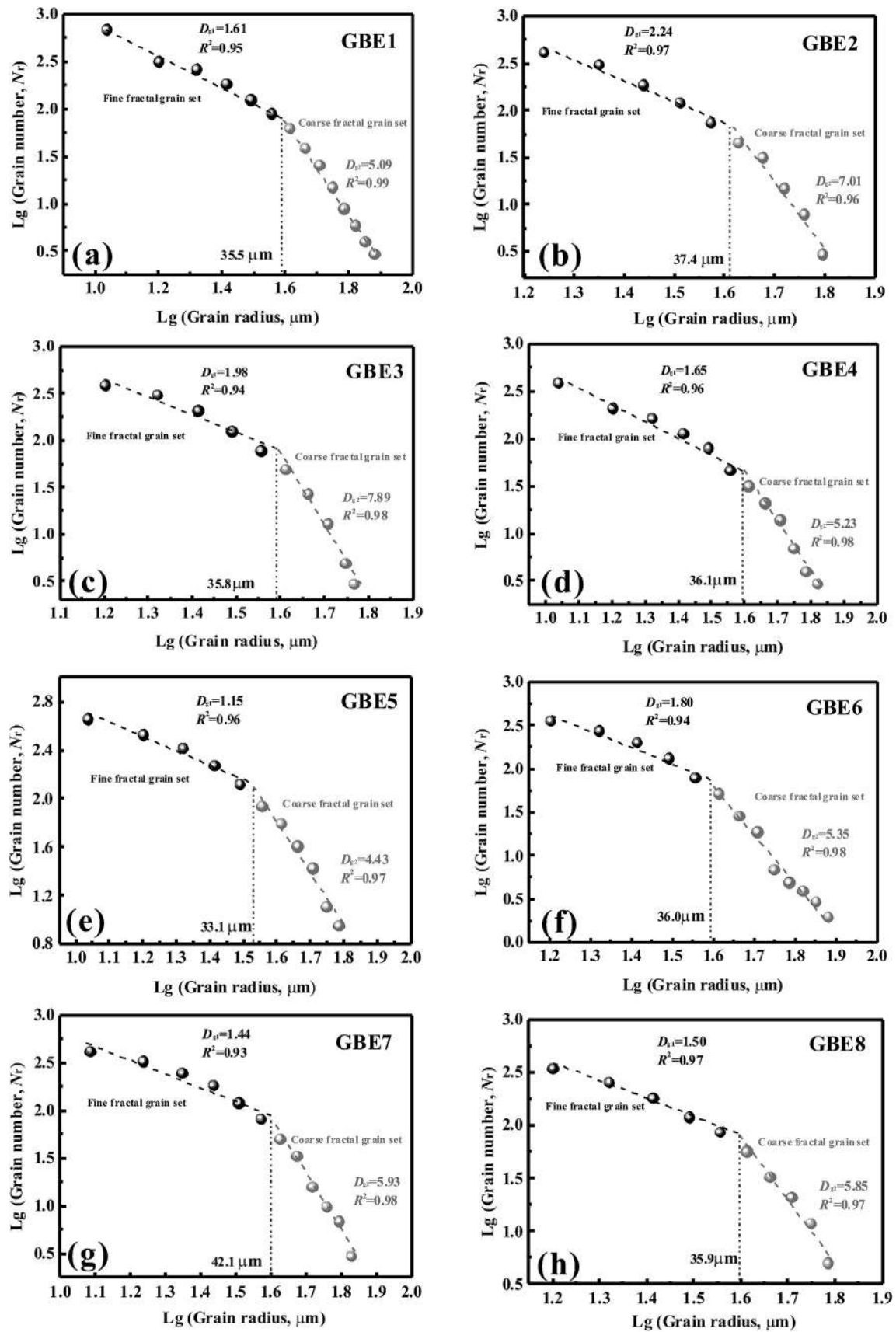
Fig. 6. Log-log plot of the cumulative number of grains versus the grain diameter of the GBE (1–8) series samples.

Table 4
Fractal dimension of the fine grain set (D_{g1}) and the coarse grain set (D_{g2}) for all GBE samples.

Sample No.	D_{g1}	D_{g2}
GBE1	1.61	5.09
GBE2	2.24	7.01
GBE3	1.98	7.89
GBE4	1.65	5.23
GBE5	1.15	4.43
GBE6	1.80	5.35
GBE7	1.44	5.93
GBE8	1.50	5.85

3.3. Intergranular corrosion test

In this section, four types of samples (GBE2, GBE6, GBE8 and GBE5) with different $F_{\Sigma3}$ were selected for the IGC test. Fig. 12 shows the relationships between the weight losses per unit surface area and the thickness loss of the four types of GBE samples in the two types of solutions as a function of corrosion time. Comparing Fig. 12(a) with Fig. 12(b), clearly, the weight loss of a GBE sample corroded in a weak acid environment is much greater than in a neutral solution. For example, the maximum weight loss after 204 h of exposure to a weakly acidic environment is 0.26 mg/mm^2, while the maximum loss in a neutral environment is 0.018 mg/mm^2. This is consistent with common perceptions. In a weak acid environment, the weight loss of corrosion of GBE2 was significantly less than that of GBE5 (Fig. 12(a)). This indicates that the GBE2 sample has the best IGC resistance, and the GBE5 sample has the worst one. For example, the weight loss of the GBE2 sample reaches 0.17 mg/mm^2, but that of the GBE5 sample reaches 0.26 mg/mm^2 when exposed for 204 h. The same trend is also observed in a neutral environment. From Sections 3.1 and 3.2, the $F_{\Sigma3}$ in GBE2 is greater than in GBE5, and the values of D_{g1} and $\Delta\alpha$ of the $\Sigma3$ GBs in GBE2 are also significantly greater than in GBE5.

The surface morphologies of GBE2 and GBE5 exposed for 12 h, 84 h, 168 h and 204 h are shown in Fig. 13, which shows no significant change in the surface of GBE2 at the beginning of corrosion (12 h) (Fig. 13(a)). Corresponding corrosion weight loss data is shown in Table 6. When exposed for 84 h, some slightly linear topography appeared on the surface of GBE2. According to Fig. 5, the GBs of these straight lines are $\Sigma3$ GBs, indicating that the linear topography is the $\Sigma3$ GBs (Fig. 13(b)). At this time, the thickness loss of the sample was approximately 7 μm, as shown in Fig. 12(c). When exposed for 168 h, the surface of GBE2 began to have a convex shape, and the surface morphologies exhibited obvious $\Sigma3$ GBs, as indicated in Fig. 13(c). When exposed for 204 h, the convex
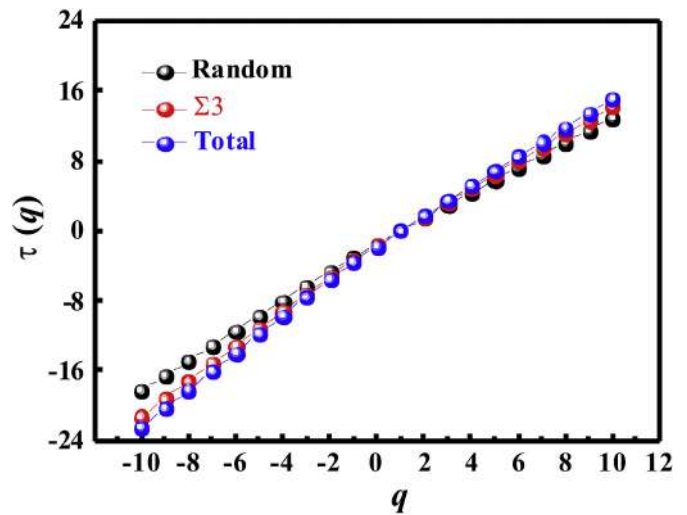
Fig. 8. Relationships between $\tau(q)$ and q of the random GB, $\Sigma3$ GB and total GB network in GBE2.

morphology of the surface became more pronounced (Fig. 13(d)). The sample thickness loss was approximately 40 μm, as shown in Fig. 12(c). According to the average grain diameter (24.6 μm) of GBE2 in Table 3, approximately 1.5 grain layers had been etched away from the surface of the sample at this time. In contrast, GBE5 is much more corrodible than GBE2. From Fig. 13(e−h), the surface of GBE5 was corroded at the initial stage of corrosion (Fig. 13(e)). When exposed for 84 h, the surface morphology of GBE5 was comparable to that of GBE2 at 168 h exposure, meaning that the degrees of convexity and concavity of the sample surface had significantly increased, as shown in Fig. 13(f). The thickness loss of the sample was 19 μm, which exceeded the half grain layer (Fig. 12(c)). According to Table 3, the average grain diameter of GBE5 was 26.7 μm. When exposed for 168 h, the linear morphology of the surface of GBE5 was significantly less than that of GBE2 based on the corrosion morphology shown in Fig. 13(g), but the surface roughness of GBE5 was greater than that of GBE2 and was roughly equivalent to the morphology GBE2 at 204 h exposure (Fig. 13(d)), meaning that the surface of the sample lost 1.5 grain layers in the thickness direction (Fig. 12(c)). When exposed for 204 h, the surface topography became severely uneven, and grain corrosion occurred (Fig. 13(h)). The average thickness loss was approximately 70 μm, which reaches 3 grain layers (Fig. 12(c)).

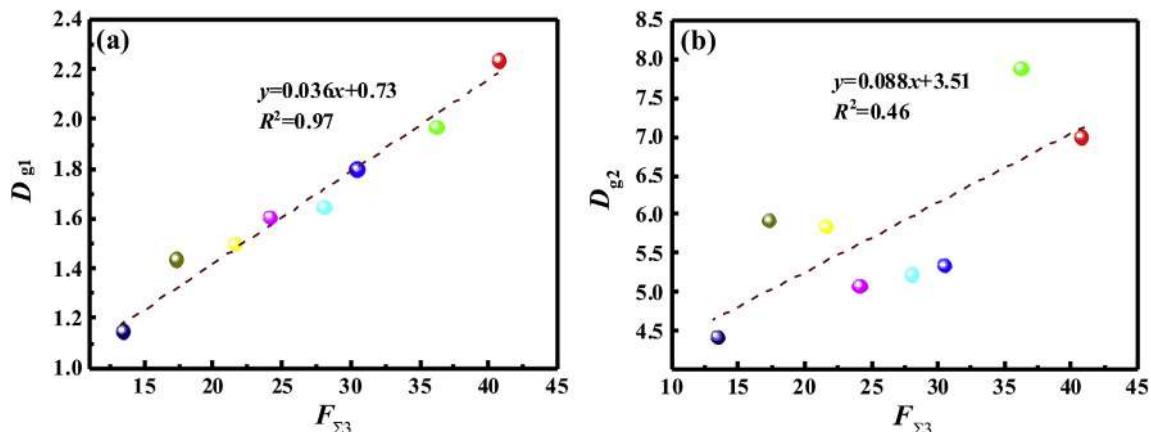In the neutral environment, no significant differences were

Fig. 7. Relationship between the fractal dimension of grains and $F_{\Sigma3}$ in the GBE samples; (a) the fine grain set; and (b) the coarse grain set.
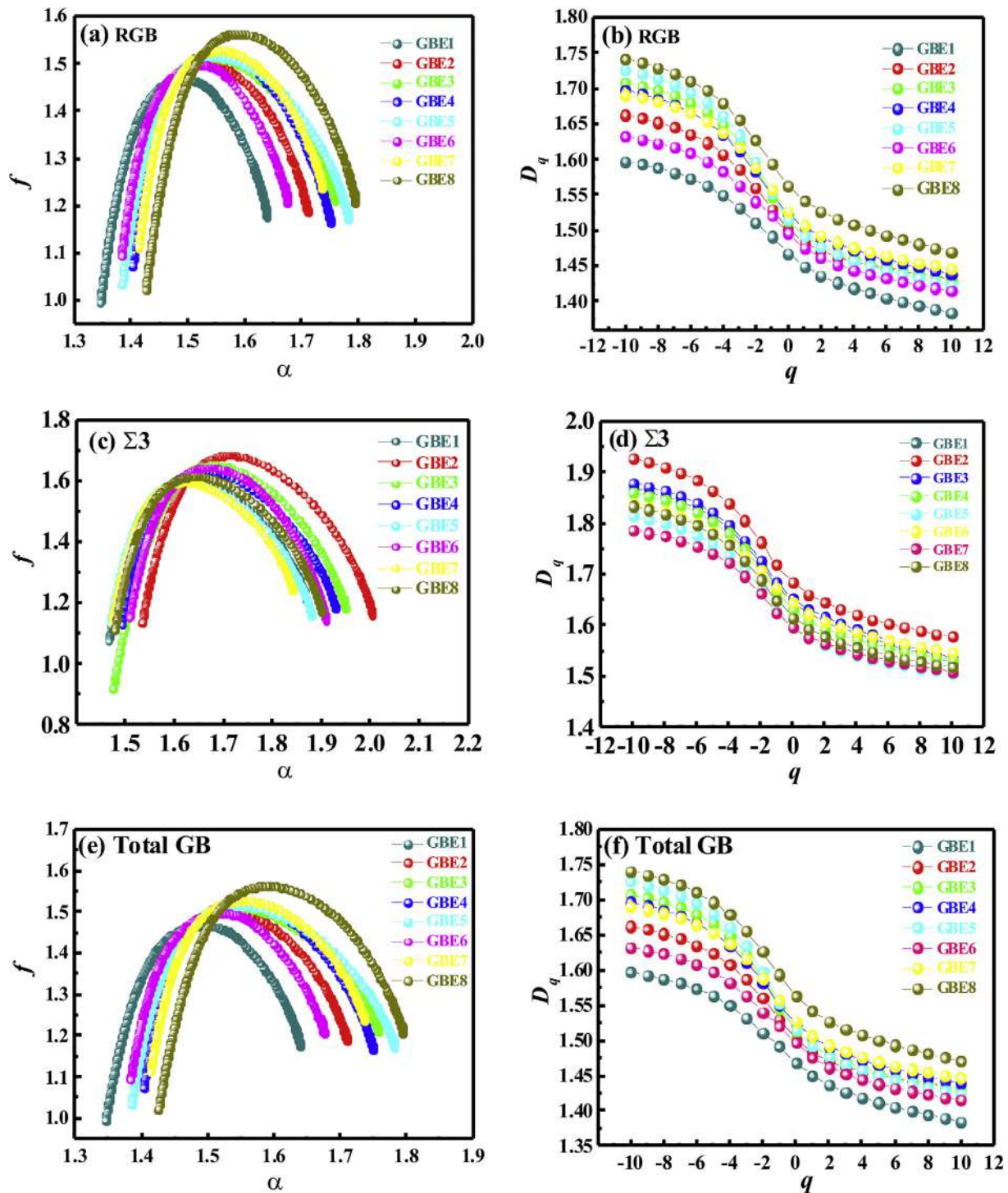
Fig. 9. Multifractal spectrum and generalized fractal spectrum of the RGB, Σ3 GBs and total GBN in the GBE (1–8) series samples; (a) (c) (e) multifractal spectra; and (b) (d) (f) generalized fractal spectra.

observed in the weight loss in the initial period (<108 h) for the four GBE samples. The weight losses of the four samples began to differ after 108 h of exposure, but with an unobvious discrepancy (Fig. 12(b)). After 156 h, the weight loss of GBE2 began to be significantly less than that of GBE5. The surface morphologies of GBE2 and GBE5 after 48 h, 108 h, 156 h and 204 h of exposure are shown in Fig. 14. The original surface morphologies of GBE2 and GBE5 were maintained until 48 h of exposure (Fig. 14(a, e)). When exposed for 108 h, corroded GBs appeared on both sample surfaces

(Fig. 14(b, f). When exposed for 156 h, the corrosion degree on the surface of GBE5 was greater than that of GBE2 (Fig. 14(c, g)). When exposed for 204 h, the corroded GB on the surface of GBE5 became thicker and deeper. In contrast, the corrosion depth of the GB of GBE2 was not as severe as that of GBE5, as shown in Fig. 14(d, h). However, for both GBE2 or GBE5, the thickness loss of the sample after exposure for 204 h did not exceed one grain layer (GBE2: ~3 μm, and GBE5: ~5 μm). Microanalysis of the chemical composition of the surface for corrosion samples will be carried out in

Table 5
The multifractal parameter ($\Delta\alpha$) and generalized fractal dimension (D_{min}) of all GBE samples.

Sample	RGB		Σ3GB		GBN	
No.	$\Delta\alpha$	D_{min}	$\Delta\alpha$	D_{min}	$\Delta\alpha$	D_{min}
GBE1	0.39	1.60	0.40	1.84	0.44	1.96
GBE2	0.40	1.66	0.48	1.93	0.49	2.04
GBE3	0.35	1.71	0.46	1.88	0.48	2.01
GBE4	0.38	1.70	0.44	1.86	0.46	1.98
GBE5	0.40	1.73	0.37	1.80	0.42	1.95
GBE6	0.40	1.66	0.45	1.87	0.47	2.00
GBE7	0.31	1.69	0.37	1.79	0.41	1.94
GBE8	0.37	1.74	0.40	1.83	0.43	1.97

future research work. Anyway, the thickness loss of the GBE2 sample is smaller than that of the GBE5 sample in both corrosion environments. For example, the thickness loss of the GBE2 sample reaches 42 μm, and the GBE5 sample reaches 68 μm in a weak acid environment. If the corrosion time lasts longer (such as one year), the difference between the two samples will be more obvious, and the superiority of the GBE2 sample to resist IGC will be more prominent.

3.4. Correlation between fractal parameters and IGC

In this section, the relationship between the multifractal parameters of Σ3GBs and the IGC resistance will be discussed in detail. From Fig. 12, corrosion weight losses and thickness loss from four GBE samples decreases gradually in both weakly acidic and neutral environments. We have obtained the $F_{\Sigma3}$ of these four samples in Section 3.1, namely, 40.69% (GBE2), 30.42% (GBE6),

21.53% (GBE8) and 13.61% (GBE5). Except for the 7.9% difference in the $F_{\Sigma3}$ between GBE8 and GBE5, the difference between the $F_{\Sigma3}$ values of the other two adjacent samples is approximately 10%. However, clearly, the difference in corrosion weight loss between GBE8 and GBE5 is much less than that between GBE2 and GBE6 or GBE6 and GBE8 according to Fig. 12. This difference shows that in addition to the $F_{\Sigma3}$, the corrosion behavior is also affected by other factors. As discussed in Section 3.1, the average grain size and the surface stress of the GBE series samples are roughly equivalent. As mentioned in Section 3.2, the size distributions of the fine grain set and the morphologies of Σ3 GBs are significantly different, meaning that the fractal dimension (D_{g1}) of the fine grain set and the multifractal structural parameter ($\Delta\alpha$) of the Σ3 GBs vary greatly among samples. This variation indicates that the grain size distribution of the fine grain set and the complex morphology of the Σ3GBs may affect the corrosion behavior more than does the $F_{\Sigma3}$.

To study the effects of structural parameters ($\Delta\alpha$ and D_{g1}) of the GBs on corrosion weight loss, the corrosion weight loss as a function of $F_{\Sigma3}$, $\Delta\alpha$ and D_{g1} for four GBE samples at different times were plotted in Fig. 15. In a weak acid environment, as shown in Fig. 15(a), the corrosion losses of the four GBE samples as a function of corrosion time (t) show different trends due to the differences in $F_{\Sigma3}$, specifically, the longer the time, the more serious the weight loss, likely due to the increasing relative surface area. Fig. 15(b and c) shows that the corrosion weight losses of the four types of samples show a continuous decrease with $\Delta\alpha$ and D_{g1}, and the longer the time, the greater the weight loss. These high correlation coefficients confirm that the structural parameters ($\Delta\alpha$ from the Σ3 GB and D_{g1}) are indeed closely related to the IGC. Note that we used a polynomial fit ($y = Ax^2 + Bx + c$) of four data points. Generally, the fitting of more than five data points is more probative, but in this
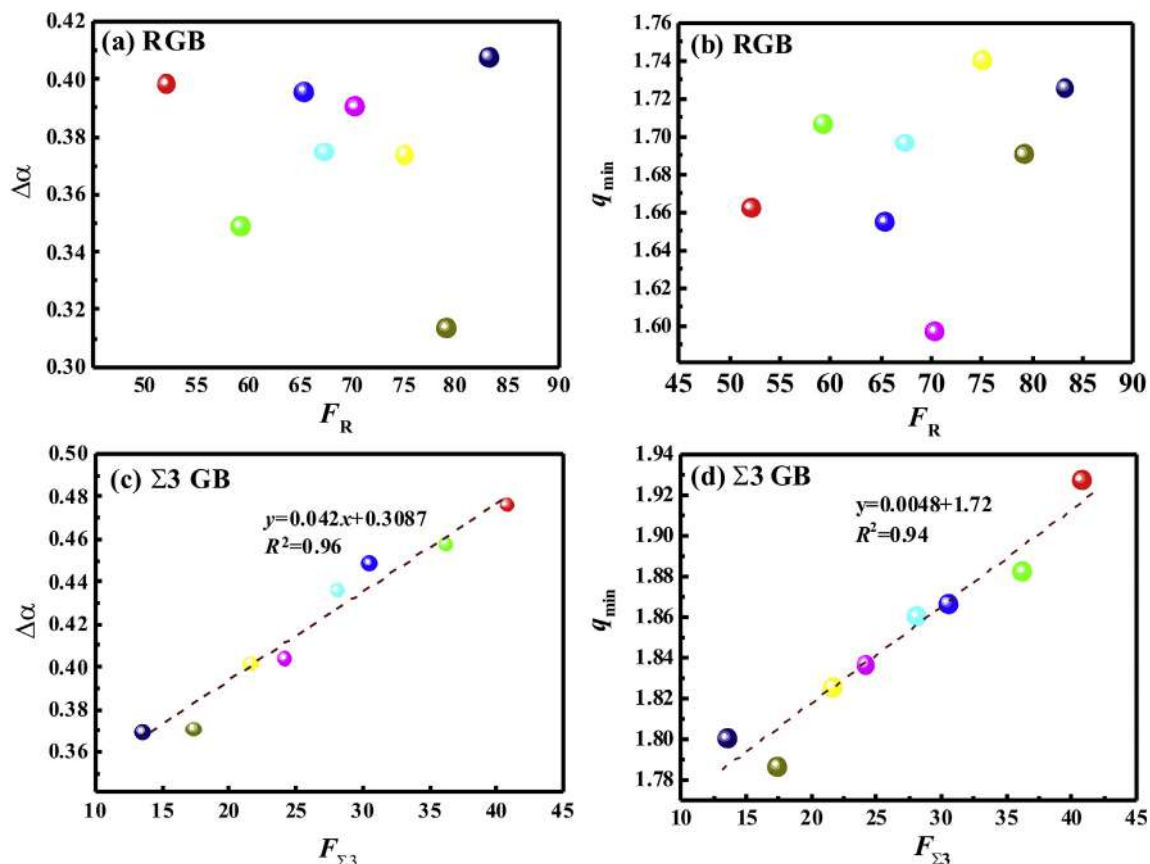

Fig. 10. Relationships between the multifractal parameters ($\Delta\alpha$) of the RGB and Σ3 GB and their fractions, respectively; (a) (b) RGB; and (c) (d) Σ3 GB.
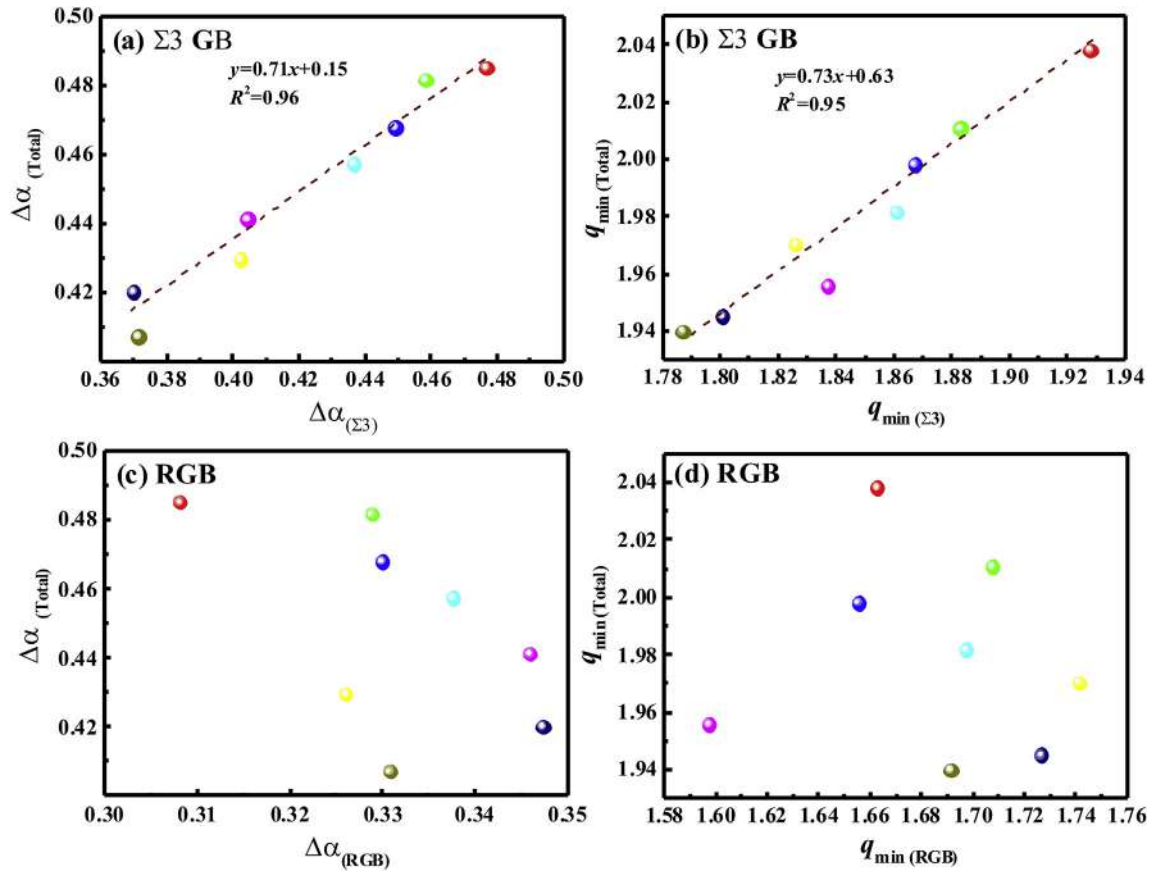
Fig. 11. Relationships between the multifractal parameters ($\Delta\alpha$) of the total GB network and the multifractal parameters of the random and $\Sigma 3$ GBs.

work, the purpose of our fitting is to see a trend, which is feasible in this case. According to the fitting formula, the larger the value of the coefficient A on the left side of the symmetry axis of the quadratic function, the greater the change in y with x. For example, after corrosion for 204 h in a weak acid environment, the corrosion loss of the four samples varies with the structural parameters ($\Delta\alpha$ and D_{g1}) of the GBs. The change in coefficient A is $A_{F\Sigma 3} < A_{Dg1} < A_{\Delta\alpha}$ ($0.0001 < 0.08 < 6.70$), as shown in Fig. 15(a–c). That is, the corrosion weight loss changes most sharply with $\Delta\alpha$, followed by D_{g1}, and finally $F_{\Sigma 3}$. Similarly, when the test was exposed to a neutral environment, although the corrosion of the sample was slower, a similar trend was observed, as shown in Fig. 15(d–f). The multifractal characteristic parameters ($\Delta\alpha$) and the fine grain fractal dimension (D_{g1}) of the GBs have the most significant influence on the corrosion weight loss of the sample. Thus, GB design based on fractal theory is essentially related to the fractal features of the fine grain set and the multifractal and generalized fractal characteristics of the $\Sigma 3$ GBs distribution, which is beneficial to control the IGC behavior of TWIP steel.

From the above reviews, D_{g1}, the complex topology of the $\Sigma 3$ GBs and the corrosion time (t) simultaneously control the weight loss and corrosion morphology. Thus, a generalized corrosion equation is established as follows. The average corrosion thickness h from Eq. (7) can be expressed as a function of structural parameters (fractal parameters) and corrosion time t:

$$h = f(fractal\ parameters,\ t)\ |_{in\ the\ same\ corrosive\ medium} \qquad (9)$$

The fractal parameters D_{g1} and $\Delta\alpha$ (from $\Sigma 3$ GBs) were found to be the dominant and sensitive structural parameters for IGC from this analysis. Thus, D_{g1}, $\Delta\alpha$, and t are used as the three input parameters to establish a quantitative relationship with h. In the

neutral environment, at the initial stage, the corrosion behavior is not dependent on both the grain structure and the GBN. The intergranular corrosion test data of the TWIP steel in the weak acid ($0.05‰$ sulfuric acid $+ 0.1$ g/L iron sulfate) solution (pH = 4.5) were used to verify the validity of Eq. (9). Using least squares fitting to the data, Eq. (9) can be further refined as

$$h = 0.27t - 37.5\Delta\alpha - 8.88D_{g1} + 24.33 \qquad (10)$$

A high correlation coefficient ($R^2 = 0.926$) from Eq. (10) suggests that Eq. (9) is valid as a generalized function, revealing the relationship between the IGC properties of a material and the fractal grain structure. The negative coefficient of $\Delta\alpha$ ($- 37.5$) and D_{g1} ($- 8.88$) quantitatively revealed that the greater the values of D_{g1} and $\Delta\alpha$ (from $\Sigma 3$ GBs), the smaller h is. Thus, the TWIP steels with high D_{g1} and $\Delta\alpha$ values will have higher IGC resistance, which is consistent with the above experimental observations (Fig. 12).

3.5. Improving IGC: A grain-boundary perspective

The optimal GBs microstructure for improving the IGC resistance of TWIP steel was discussed above. Section 3.4 has shown that the corrosion weight loss of a GBE specimen is most sensitive to the change of the multifractal parameter ($\Delta\alpha$) of the $\Sigma 3$ GBs, while $\Delta\alpha$ is subjected to $F_{\Sigma 3}$, and $F_{\Sigma 3}$ is affected by the fractal dimension (D_{g1}) of the fine grain set (<36 μm), meaning that the multifractal characteristic parameter $\Delta\alpha$, the fine grain fractal dimension D_{g1} and $F_{\Sigma 3}$ are mutually constrained and together affect the IGC properties of austenitic steel. Fig. 16 reveals the relationship between D_{g1}, $F_{\Sigma 3}$ and $\Delta\alpha$. As shown, when $\Delta\alpha$, $F_{\Sigma 3}$ and D_{g1} increase simultaneously, the corrosion resistance of TWIP steel can increase.
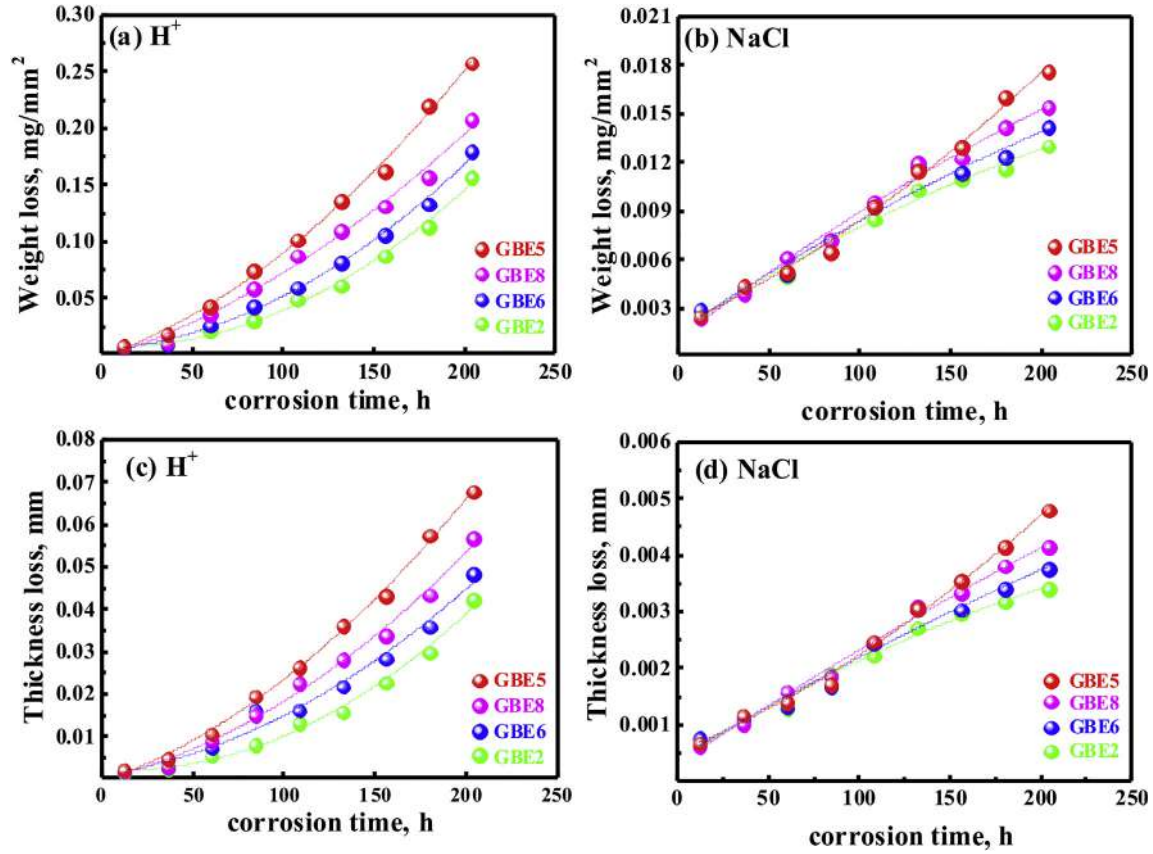
Fig. 12. Correlations between corrosion weight loss as well as thickness loss and corrosion time for four GBE (2, 6, 8, and 5) samples in two environments: (a) (c) acidic environment; and (b) (d) neutral environment.
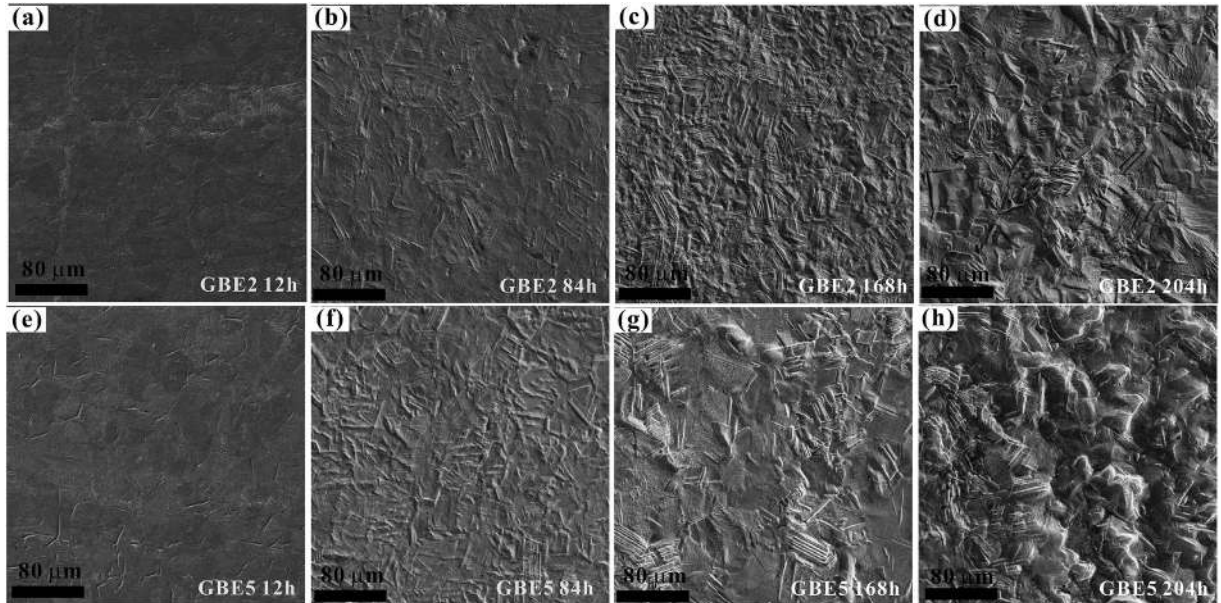

Fig. 13. Morphological maps of GBE2 and GBE5 samples after corrosion in a weakly acidic environment for different times; (a–d) GBE2; and (e–g) GBE5.

In contrast, TWIP steel has the least corrosion resistance. To quantitatively obtain the correlation between D_{g1}, $F_{\Sigma3}$ and $\Delta\alpha$ of the $\Sigma3$ GBs, the least squares fit is used:

$$F_{\Sigma3} = 14.84D_{g1} + 109.21\Delta\alpha - 44.23 \tag{11}$$

A high correlation coefficient ($R^2 = 0.998$) from Eq. (11) suggests that even under the same $F_{\Sigma3}$ value, D_{g1} and $\Delta\alpha$ may be different and thereby yield different levels of IGC resistance. Thus, GB design coupled with morphological analysis based on fractal theory can more accurately predict and control the IGC resistance of austenitic steel.

Table 6
Weight loss date with standard deviation of four GBE samples in two corrosion environments.

Sample	GBE2		GBE6		GBE8		GBE5	
mg/mm^2	H$^+$	NaCl	H$^+$	NaCl	H$^+$	NaCl	H$^+$	NaCl
12 h	0.0056 ± 0.0002	0.0027 ± 0.0001	0.0063 ± 0.0002	0.0029 ± 0.0001	0.0076 ± 0.0003	0.0024 ± 0.0001	0.0077 ± 0.0002	0.0025 ± 0.0001
36 h	0.0089 ± 0.0003	0.0040 ± 0.0001	0.0098 ± 0.0004	0.0042 ± 0.0001	0.0102 ± 0.0004	0.0039 ± 0.0001	0.0185 ± 0.0007	0.0044 ± 0.0001
60 h	0.0213 ± 0.0012	0.0049 ± 0.0001	0.0262 ± 0.0013	0.0051 ± 0.0001	0.0361 ± 0.0021	0.0061 ± 0.0001	0.0431 ± 0.0024	0.0053 ± 0.0001
84 h	0.0302 ± 0.0016	0.0072 ± 0.0001	0.0432 ± 0.0022	0.0065 ± 0.0001	0.0586 ± 0.0033	0.0072 ± 0.0002	0.0740 ± 0.0037	0.0065 ± 0.0002
108 h	0.0491 ± 0.0033	0.0084 ± 0.0002	0.0592 ± 0.0038	0.0094 ± 0.0002	0.0876 ± 0.0054	0.0095 ± 0.0002	0.1018 ± 0.0064	0.0093 ± 0.0003
132 h	0.0615 ± 0.0039	0.0103 ± 0.0002	0.0818 ± 0.0052	0.0117 ± 0.0003	0.1096 ± 0.0073	0.0120 ± 0.0003	0.1359 ± 0.0084	0.0115 ± 0.0003
156 h	0.0877 ± 0.0063	0.0110 ± 0.0004	0.1061 ± 0.0077	0.0114 ± 0.0004	0.1310 ± 0.0095	0.0123 ± 0.0004	0.1622 ± 0.0127	0.0129 ± 0.0005
180 h	0.1129 ± 0.0078	0.0116 ± 0.0004	0.1328 ± 0.0085	0.0123 ± 0.0004	0.1568 ± 0.0108	0.0142 ± 0.0004	0.2199 ± 0.0166	0.0160 ± 0.0005
204 h	0.1566 ± 0.0093	0.0131 ± 0.0005	0.1798 ± 0.0102	0.0142 ± 0.0005	0.2081 ± 0.0132	0.0154 ± 0.0005	0.2578 ± 0.0190	0.0176 ± 0.0006
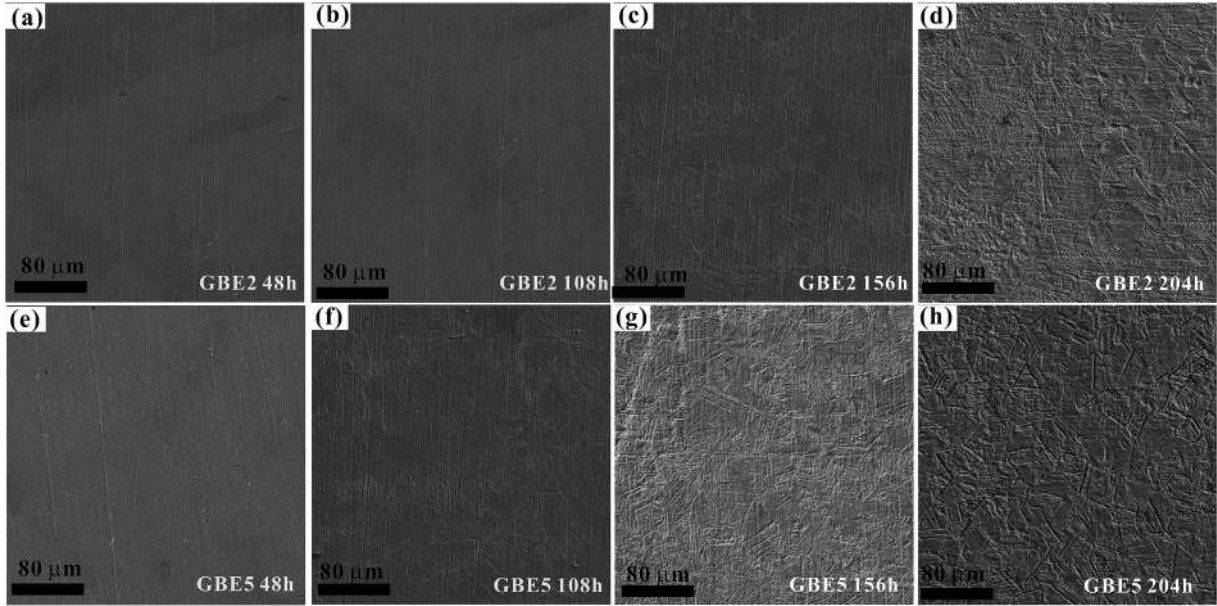
Fig. 14. Morphological maps of GBE2 and GBE5 samples after corrosion in a neutral environment for different times: (a−d) GBE2; (e−g) GBE5.
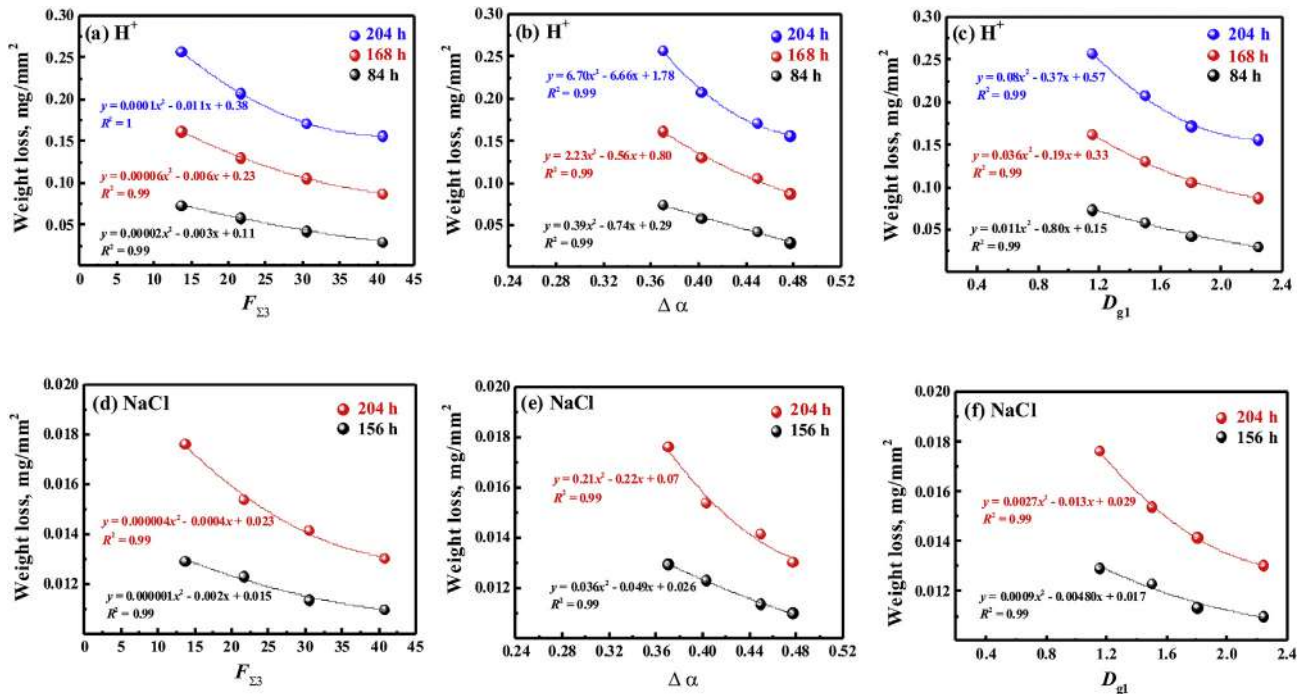
Fig. 15. Relationships between the weight loss of four GBE samples in two different environments and the fraction of Σ3 GBs, the multifractal parameter and the grain fractal dimension of the fine grain set in (a−c) the weakly acidic environment and (d−e) the neutral environment.
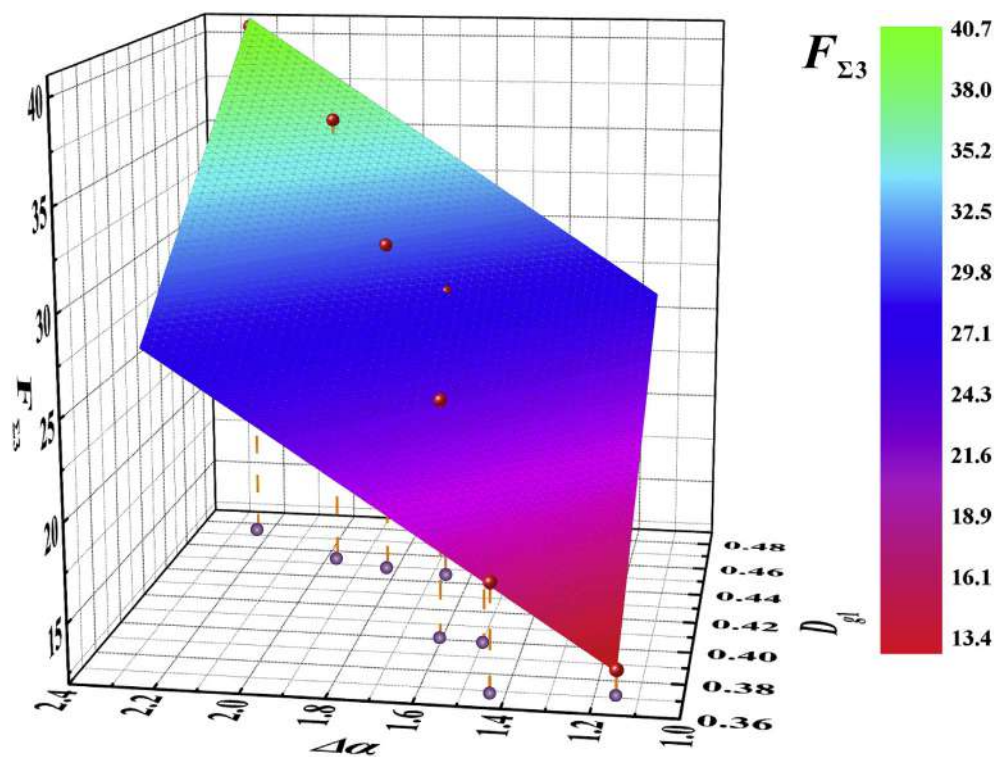
Fig. 16. Relationships between the fraction of Σ3 GBs, the multifractal parameter and the grain fractal dimension of the fine grain set in TWIP steel.

4. Conclusions

The correlations between the structural parameters and fractions of the three types of GB were established based on fractal theories. Furthermore, the dependences of the IGC properties on grain size distribution as well as on the Σ3 GBs distribution characteristics were studied based on an IGC test by the weight loss method. The results show that the GB design method coupled with morphological analysis based on fractal theory may provide a new avenue to predict and control the IGC properties of austenitic steel more accurately. The main conclusions drawn are as follows:

1. For the corrosion test, the GBE series samples of TWIP steel have different degrees of corrosion in both environments. With increasing time, the degree of corrosion of the GBE sample exhibits significant GB dependence;
2. The grain size distribution of TWIP steel satisfy the double fractal feature and are divided into two typical grain sets: the fine grain set and the coarse grain set. For all samples, a critical grain diameter (~36 μm) exists between the two fractal grain sets. This critical value may be an inherent property of the material. The distribution of fine grains (<36 μm) in TWIP steel samples has natural fractal characteristics and satisfies a good linear correlation with the $F_{\Sigma 3}$;
3. The distribution characteristics of RGBs, Σ3 GBs and total GBN of TWIP steel meet multifractal fractal features. $F_{\Sigma 3}$ has a good linear correlation with its multifractal parameters. However, no significant relevant relationships were found between F_{RGB} and its multifractal parameters ($\Delta\alpha$) or between the $\Delta\alpha$ and D_{min} values of RGB and those of total GBN. Furthermore, a good positive correlation was found between the $\Delta\alpha$ and D_{min} values of Σ3 GB and those of total GBN, indicating that Σ3 GBs control the overall complexity of total GBN in TWIP steels;
4. A quantitative relationship equation for corrosion was proposed and verified as a function of the fractal structural parameters ($\Delta\alpha$ and D_{g1}) and corrosion time (t), that is, $h = 0.27t\text{-}37.5\Delta\alpha\text{-}$

$8.88D_{g1}+24.33$. In this case, $\Delta\alpha$ of Σ3 GBs and D_{g1} are sensitive structural parameters that control the corrosion behavior in TWIP steel. In particular, high values of $\Delta\alpha$ and D_{g1} will yield a lower average corrosion thickness and hence higher IGC resistance. The correlation between the three structural parameters ($\Delta\alpha$, D_{g1}, and $F_{\Sigma 3}$) was established by least squares linear regression to be $F_{\Sigma 3} = 14.84D_{g1}+109.21\Delta\alpha\text{-}44.23$, which shows that TWIP steels with higher $\Delta\alpha$, D_{g1} and $F_{\Sigma 3}$ values of the Σ3 GBs will show higher resistance to IGC.

Based on this work, we believe a grain size of less than 36 μm may be a critical diameter for improving the IGC properties of TWIP steel. Below this size, more Σ3 GBs can be obtained by GBE, thereby reducing the IGC rate, which is not easy to achieve when the grain size is greater than 36 μm. At the same time, the preparation of TWIP steel with a highly complex distribution of Σ3 GBs can also improve IGC properties.

Data availability statement

The raw/processed data required to reproduce these findings cannot be shared at this time as the data also forms part of an ongoing study.

CRediT authorship contribution statement

Hao Fu: Conceptualization, Investigation, Writing - original draft. **Wei Wang:** Investigation. **Xiaojun Chen:** Conceptualization, Methodology, Software, Writing - review & editing. **Giorgio Pia:** Visualization, Writing - review & editing. **Jinxu Li:** Funding acquisition, Project administration, Resources.

Acknowledgments

Appendix A. Supplementary data

Supplementary data to this article can be found online at https://doi.org/10.1016/j.matdes.2019.108253.

References

[1] T. Watanabe, An approach to grain-boundary design for strong and ductile polycrystals, Res. Mech. 11 (1) (1984) 47–84.

[2] E.M. Lehockey, A.M. Brennenstuhl, I. Thompson, On the relationship between grain boundary connectivity, coincident site lattice boundaries, and intergranular stress corrosion cracking, Corros. Sci. 46 (10) (2004) 2383–2404, https://doi.org/10.1016/j.corsci.2004.01.019.

[3] U. Krupp, W.M. Kane, X. Liu, O. Dueber, C. Laird, C.J. McMahon, The effect of grain-boundary-engineering-type processing on oxygen-induced cracking of IN718, Mater. Sci. Eng. A 349 (1) (2003) 213–217, https://doi.org/10.1016/S0921-5093(02)00753-0.

[4] M. Qian, J.C. Lippold, The effect of annealing twin-generated special grain boundaries on HAZ liquation cracking of nickel-base superalloys, Acta Mater. 51 (12) (2003) 3351–3361, https://doi.org/10.1016/S1359-6454(03)00090-9.

[5] V. Thaveeprungsriporn, G.S. Was, The role of coincidence-site-lattice boundaries in creep of Ni-16Cr-9Fe at 360 °C, Metall. Mater. Trans. A 28 (10) (1997) 2101–2112, https://doi.org/10.1007/s11661-997-0167-6.

[6] Y.J. Kwon, S.-P. Jung, B.-J. Lee, C.S. Lee, Grain boundary engineering approach to improve hydrogen embrittlement resistance in Fe Mn C TWIP steel, Int. J. Hydrogen Energy 43 (21) (2018) 10129–10140, https://doi.org/10.1016/j.ijhydene.2018.04.048.

[7] Y.J. Kwon, H.J. Seo, J.N. Kim, C.S. Lee, Effect of grain boundary engineering on hydrogen embrittlement in Fe-Mn-C TWIP steel at various strain rates, Corros. Sci. 142 (2018) 213–221, https://doi.org/10.1016/j.corsci.2018.07.028.

[8] H. Fu, W. Wang, H. Zhao, F. Jin, J. Li, Study of hydrogen-induced delayed fracture in high-Mn TWIP/TRIP steels during in situ electrochemical hydrogen-charging: role of microstructure and strain rate in crack initiation and propagation, Corros. Sci. (2019) 108191, https://doi.org/10.1016/j.corsci.2019.108191.

[9] D.H. Warrington, P. Bufalini, The coincidence site lattice and grain boundaries, Scr. Metall. 5 (9) (1971) 771–776, https://doi.org/10.1016/0036-9748(71)90161-X.

[10] S. Kobayashi, T. Maruyama, S. Tsurekawa, T. Watanabe, Grain boundary engineering based on fractal analysis for control of segregation-induced intergranular brittle fracture in polycrystalline nickel, Acta Mater. 60 (17) (2012) 6200–6212, https://doi.org/10.1016/j.actamat.2012.07.065.

[11] V. Randle, The Role of the Coincidence Site Lattice in Grain Boundary Engineering, Maney, 1996.

[12] C. Prasad, P. Bhuyan, C. Kaithwas, R. Saha, S. Mandal, Microstructure engineering by dispersing nano-spheroid cementite in ultrafine-grained ferrite and its implications on strength-ductility relationship in high carbon steel, Mater. Des. 139 (2018) 324–335, https://doi.org/10.1016/j.matdes.2017.11.019.

[13] T. Liu, S. Xia, B. Wang, Q. Bai, B. Zhou, C. Su, Grain orientation statistics of grain-clusters and the propensity of multiple-twinning during grain boundary engineering, Mater. Des. 112 (2016) 442–448, https://doi.org/10.1016/j.matdes.2016.09.079.

[14] M. Masoumi, L.P.M. Santos, I.N. Bastos, S.S.M. Tavares, M.J.G. da Silva, H.F.G. de Abreu, Texture and grain boundary study in high strength Fe–18Ni–Co steel related to hydrogen embrittlement, Mater. Des. 91 (2016) 90–97, https://doi.org/10.1016/j.matdes.2015.11.093.

[15] H.B. Li, Z.H. Jiang, H. Feng, S.C. Zhang, L. Li, P.D. Han, R.D.K. Misra, J.Z. Li, Microstructure, mechanical and corrosion properties of friction stir welded high nitrogen nickel-free austenitic stainless steel, Mater. Des. 84 (2015) 291–299, https://doi.org/10.1016/j.matdes.2015.06.103.

[16] D. Song, C. Li, N. Liang, F. Yang, J. Jiang, J. Sun, G. Wu, A. Ma, X. Ma, Simultaneously improving corrosion resistance and mechanical properties of a magnesium alloy via equal-channel angular pressing and post water annealing, Mater. Des. 166 (2019) 107621, https://doi.org/10.1016/j.matdes.2019.107621.

[17] Z.X. Yang, B. Kan, J.X. Li, Y.J. Su, L.J. Qiao, Hydrostatic pressure effects on stress corrosion cracking of X70 pipeline steel in a simulated deep-sea environment, Int. J. Hydrogen Energy 42 (44) (2017) 27446–27457, https://doi.org/10.1016/j.ijhydene.2017.09.061.

[18] P.E.J. Flewitt, R.K. Wild, Grain boundaries: their microstructure and chemistry, in: P.E.J. Flewitt, R.K. Wild (Eds.), Grain Boundaries: Their Microstructure and Chemistry, Wiley-VCH, 2001, p. 338. ISBN 0-471-97951-1, April 2001.

[19] D. An, T.A. Griffiths, P. Konijnenberg, S. Mandal, Z. Wang, S. Zaefferer, Correlating the five parameter grain boundary character distribution and the intergranular corrosion behaviour of a stainless steel using 3D orientation microscopy based on mechanical polishing serial sectioning, Acta Mater. 156 (2018) 297–309, https://doi.org/10.1016/j.actamat.2018.06.044.

[20] S. Kumar, B.S. Prasad, V. Kain, J. Reddy, Methods for making alloy 600 resistant to sensitization and intergranular corrosion, Corros. Sci. 70 (2013) 55–61, https://doi.org/10.1016/j.corsci.2012.12.021.

[21] M.-L. de Bonfils-Lahovary, C. Josse, L. Laffont, C. Blanc, Influence of hydrogen on the propagation of intergranular corrosion defects in 2024 aluminium alloy, Corros. Sci. 148 (2019) 198–205, https://doi.org/10.1016/j.corsci.2018.12.019.

[22] Z. Wang, F. Zhu, K. Zheng, J. Jia, Y. Wei, H. Li, L. Huang, Z. Zheng, Effect of the thickness reduction on intergranular corrosion in an under−aged Al−Mg−Si−Cu alloy during cold−rolling, Corros. Sci. 142 (2018) 201−212, https://doi.org/10.1016/j.corsci.2018.07.018.

[23] S.K. Kairy, S. Turk, N. Birbilis, A. Shekhter, The role of microstructure and microchemistry on intergranular corrosion of aluminium alloy AA7085-T7452, Corros. Sci. 143 (2018) 414−427, https://doi.org/10.1016/j.corsci.2018.08.033.

[24] S. Xia, H. Li, T.G. Liu, B.X. Zhou, Appling grain boundary engineering to Alloy 690 tube for enhancing intergranular corrosion resistance, J. Nucl. Mater. 416 (3) (2011) 303−310, https://doi.org/10.1016/j.jnucmat.2011.06.017.

[25] M. Michiuchi, H. Kokawa, Z.J. Wang, Y.S. Sato, K. Sakai, Twin-induced grain boundary engineering for 316 austenitic stainless steel, Acta Mater. 54 (19) (2006) 5179−5184, https://doi.org/10.1016/j.actamat.2006.06.030.

[26] S.K. Pradhan, P. Bhuyan, S. Mandal, Individual and synergistic influences of microstructural features on intergranular corrosion behavior in extra-low carbon type 304L austenitic stainless steel, Corros. Sci. 139 (2018) 319−332, https://doi.org/10.1016/j.corsci.2018.05.014.

[27] C. Hu, S. Xia, H. Li, T. Liu, B. Zhou, W. Chen, N. Wang, Improving the intergranular corrosion resistance of 304 stainless steel by grain boundary network control, Corros. Sci. 53 (5) (2011) 1880−1886, https://doi.org/10.1016/j.corsci.2011.02.005.

[28] B.B. Mandelbrot, D.E. Passoja, A.J. Paullay, Fractal character of fracture surfaces of metals, Nature 308 (5961) (1984) 721−722, https://doi.org/10.1038/308721a0.

[29] I. Farina, R. Goodall, E. Hernández-Nava, A. di Filippo, F. Colangelo, F. Fraternali, Design, microstructure and mechanical characterization of Ti6Al4V reinforcing elements for cement composites with fractal architecture, Mater. Des. 172 (2019) 107758, https://doi.org/10.1016/j.matdes.2019.107758.

[30] J. Wang, Y. Zhang, N. He, C.H. Wang, Crashworthiness behavior of Koch fractal structures, Mater. Des. 144 (2018) 229−244, https://doi.org/10.1016/j.matdes.2018.02.035.

[31] M. Aureli, A.S.M. Alzaabi, A.G.S. Hussien, C.C. Doumanidis, S.M. Jaffar, I.E. Gunduz, C. Rebholz, N. Kostoglou, Y. Liao, C.C. Doumanidis, Thermostructural observation and adaptive control of fractal structure in ball-milled materials, Mater. Des. 160 (2018) 772−782, https://doi.org/10.1016/j.matdes.2018.10.010.

[32] O.A. Hilders, M. Ramos, N.D. Peña, L. Sàenz, Fractal geometry of fracture surfaces of a duplex stainless steel, J. Mater. Sci. 41 (17) (2006) 5739−5742, https://doi.org/10.1007/s10853-006-0102-z.

[33] H. Fu, W. Wang, X. Chen, G. Pia, J. Li, Fractal and multifractal analysis of fracture surfaces caused by hydrogen embrittlement in high-Mn twinning/transformation-induced plasticity steels, Appl. Surf. Sci. 470 (2019) 870−881, https://doi.org/10.1016/j.apsusc.2018.11.179.

[34] X. Chen, G. Yao, An improved model for permeability estimation in low permeable porous media based on fractal geometry and modified Hagen-Poiseuille flow, Fuel 210 (2017) 748−757, https://doi.org/10.1016/j.fuel.2017.08.101.

[35] X. Chen, G. Yao, C. Luo, P. Jiang, J. Cai, K. Zhou, E. Herrero-Bervera, Capillary pressure curve determination based on a 2-D cross-section analysis via fractal geometry: a bridge between 2-D and 3-D pore structure of porous media, J. Geophys. Res. Sol. Ea 124 (2019) 2352−2367, https://doi.org/10.1029/2018jb016722.

[36] G. Pia, L. Casnedi, R. Ricciu, L.A. Besalduch, O. Cocco, A. Murru, P. Meloni, U. Sanna, Thermal properties of porous stones in cultural heritage: experimental findings and predictions using an intermingled fractal units model, Energy Build. 118 (2016) 232−239, https://doi.org/10.1016/j.enbuild.2016.03.011.

[37] G. Pia, M. Carta, F. Delogu, Nanoporous Au foams: variation of effective Young's modulus with ligament size, Scr. Mater. 144 (2018) 22−26, https://doi.org/10.1016/j.scriptamat.2017.09.038.

[38] G. Pia, U. Sanna, An intermingled fractal units model to evaluate pore size distribution influence on thermal conductivity values in porous materials, Appl. Therm. Eng. 65 (1) (2014) 330−336, https://doi.org/10.1016/j.applthermaleng.2014.01.037.

[39] X. Chen, G. Yao, E. Herrero-Bervera, J. Cai, K. Zhou, C. Luo, P. Jiang, J. Lu, A new model of pore structure typing based on fractal geometry, Mar. Pet. Geol. 98 (2018) 291−305, https://doi.org/10.1016/j.marpetgeo.2018.08.023.

[40] S. Kobayashi, R. Kobayashi, T. Watanabe, Control of grain boundary connectivity based on fractal analysis for improvement of intergranular corrosion resistance in SUS316L austenitic stainless steel, Acta Mater. 102 (2016) 397−405, https://doi.org/10.1016/j.actamat.2015.08.075.

[41] C.K. Kaithwas, P. Bhuyan, S.K. Pradhan, S. Mandal, Microstructure evolution during low-strain thermo-mechanical processing and its repercussion on intergranular corrosion in alloy 600H, Mater. Char. 145 (2018) 582−593, https://doi.org/10.1016/j.matchar.2018.09.019.

[42] A. Mohammadi, M. Koyama, G. Gerstein, H.J. Maier, H. Noguchi, Hydrogen-assisted failure in a bimodal twinning-induced plasticity steel: delamination events and damage evolution, Int. J. Hydrogen Energy 43 (4) (2018) 2492−2502, https://doi.org/10.1016/j.ijhydene.2017.11.177.

[43] B.C. De Cooman, Y. Estrin, S.K. Kim, Twinning-induced plasticity (TWIP) steels, Acta Mater. (2017), https://doi.org/10.1016/j.actamat.2017.06.046.

[44] Z.Y. Liang, X. Wang, W. Huang, M.X. Huang, Strain rate sensitivity and evolution of dislocations and twins in a twinning-induced plasticity steel, Acta

Mater. 88 (2015) 170–179, https://doi.org/10.1016/j.actamat.2015.01.013.

[45] S.-M. Lee, S.-J. Lee, S. Lee, J.-H. Nam, Y.-K. Lee, Tensile properties and deformation mode of Si-added Fe-18Mn-0.6C steels, Acta Mater. 144 (2018) 738–747, https://doi.org/10.1016/j.actamat.2017.11.023.

[46] J.H. Choi, M.C. Jo, H. Lee, A. Zargaran, T. Song, S.S. Sohn, N.J. Kim, S. Lee, Cu addition effects on TRIP to TWIP transition and tensile property improvement of ultra-high-strength austenitic high-Mn steels, Acta Mater. 166 (2019) 246–260, https://doi.org/10.1016/j.actamat.2018.12.044.

[47] A.S. Hamada, P. Sahu, D.A. Porter, Indentation property and corrosion resistance of electroless nickel–phosphorus coatings deposited on austenitic high-Mn TWIP steel, Appl. Surf. Sci. 356 (2015) 1–8, https://doi.org/10.1016/j.apsusc.2015.07.153.

[48] I.-J. Park, S.-M. Lee, M. Kang, S. Lee, Y.-K. Lee, Pitting corrosion behavior in advanced high strength steels, J. Alloy. Comp. 619 (2015) 205–210, https://doi.org/10.1016/j.jallcom.2014.08.243.

[49] M.B. Kannan, R.K.S. Raman, S. Khoddam, S. Liyanaarachchi, Corrosion behavior of twinning-induced plasticity (TWIP) steel, Mater. Corros. 64 (3) (2013) 231–235, https://doi.org/10.1002/maco.201106356.

[50] A.S. Hamada, L.P. Karjalainen, Corrosion behaviour of high-Mn TWIP steels with electroless Ni-P coating, Open Corros. J. 3 (1) (2010) 1–6, https://doi.org/10.2174/1876503301003010001.

[51] A. Grajcar, S. Kołodziej, W. Krukiewicz, Corrosion resistance of high-manganese austenitic steels, Archiv. Mater. Sci. Eng41 (2) (2010) 77–84.

[52] T. Watanabe, H. Fujii, H. Oikawa, K.I. Arai, Grain boundaries in rapidly solidified and annealed Fe-6.5 mass% Si polycrystalline ribbons with high ductility, Acta Metall. 37 (3) (1989) 941–952, https://doi.org/10.1016/0001-6160(89)90021-7.

[53] A. Rabbani, S. Jamshidi, S. Salehi, An automated simple algorithm for realistic pore network extraction from micro-tomography images, J. Pet. Sci. Eng. 123 (2014) 164–171, https://doi.org/10.1016/j.petrol.2014.08.020.

[54] H.G.E. Hentschel, I. Procaccia, The infinite number of generalized dimensions of fractals and strange attractors, Phys. D Nonlinear Phenom. 8 (3) (1983) 435–444, https://doi.org/10.1016/0167-2789(83)90235-X.

[55] H. Salat, R. Murcio, E. Arcaute, Multifractal methodology, Physica A: Stat. Mech. Appl. 473 (2017) 467–487, https://doi.org/10.1016/j.physa.2017.01.041.

[56] H. Xie, H. Sun, Y. Ju, Z. Feng, Study on generation of rock fracture surfaces by using fractal interpolation, Int. J. Solids Struct. 38 (32) (2001) 5765–5787, https://doi.org/10.1016/S0020-7683(00)00390-5.